

# Drift-Diffusion Matching: Embedding dynamics in latent manifolds of asymmetric neural networks

Ramón Nartallo-Kaluarachchi\*,†, Renaud Lambiotte\*,‡, and Alain Goriely\*

\*Mathematical Institute, University of Oxford, Woodstock Road, Oxford, OX2 6GG, United Kingdom

†Centre for Eudaimonia and Human Flourishing, University of Oxford, 7 Stoke Pl, Oxford, OX3 9BX, United Kingdom

‡Complexity Science Hub, Metternichgasse 8, Vienna, 1030, Austria

{ramon.nartallo-kaluarachchi}{renaud.lambiotte}{alain.goriely}@maths.ox.ac.uk

(Dated: February 17, 2026)

Recurrent neural networks (RNNs) provide a theoretical framework for understanding computation in biological neural circuits, yet classical results, such as Hopfield’s model of associative memory, rely on symmetric connectivity that restricts network dynamics to gradient-like flows. In contrast, biological networks support rich time-dependent behaviour facilitated by their asymmetry. Here we introduce a general framework, which we term drift–diffusion matching, for training continuous-time RNNs to represent arbitrary stochastic dynamical systems within a low-dimensional latent subspace. Allowing asymmetric connectivity, we show that RNNs can faithfully embed the drift and diffusion of a given stochastic differential equation, including nonlinear and nonequilibrium dynamics such as chaotic attractors. As an application, we construct RNN realisations of stochastic systems that transiently explore various attractors through both input-driven switching and autonomous transitions driven by nonequilibrium currents, which we interpret as models of associative and sequential (episodic) memory. To elucidate how these dynamics are encoded in the network, we introduce decompositions of the RNN based on its asymmetric connectivity and its time-irreversibility. Our results extend attractor neural network theory beyond equilibrium, showing that asymmetric neural populations can implement a broad class of dynamical computations within low-dimensional manifolds, unifying ideas from associative memory, nonequilibrium statistical mechanics, and neural computation.

## I. INTRODUCTION

Understanding how populations of neurons encode information and perform computations is one of the most significant problems in neuroscience [1]. Central to the ‘connectionist’ perspective, is the idea that cognition is performed by distributed networks of interacting neurons. However, unlike the feed-forward architectures that dominate modern machine learning, the neuronal networks of the brain are recurrent, leading to a rich repertoire of time-evolving dynamics. As a result, classes of *recurrent neural networks* (RNNs) have become the prototypical models for dynamic computation in biological neural circuits [2]. These networks, and variants thereof, have been used extensively to model neural data [3, 4], develop theories of neural computation [5, 6], as well as perform sequence learning tasks, such as the prediction and encoding of chaotic time-series [7–9].

One of the most influential results in the study of RNNs is Hopfield’s model of associative memory [10, 11]. In the continuous version of the model, the dynamics are identical to that of a so-called ‘vanilla’ RNN. Such a system is composed of  $n$  neurons, each with internal state  $u_i$  and output state  $v_i = h(u_i)$ , where  $h$  is a monotonic nonlinear activation function (we will take  $h(x) = \tanh(x)$ ). The dynamics of the internal state are given by the stochastic differential equation (SDE),

$$d\mathbf{u}(t) = \mathbf{F}(\mathbf{u}) dt + B d\mathbf{w}(t), \quad (1)$$

where  $\mathbf{u} = (u_1, \dots, u_n)$  and  $\mathbf{F} = (F_1, \dots, F_n)$  is the *drift* function, with,

$$F_i = -u_i + \sum_j W_{ij} v_j + I_i. \quad (2)$$

Here  $B \in \mathbb{R}^{n \times d}$  and  $\mathbf{w}(t)$  is a Wiener process with  $d$  independent sources of noise [12]. We also define  $\Upsilon = BB^\top/2$  to be

the positive semidefinite *diffusion matrix* of rank  $d$ . The connectivity from neuron  $j$  to neuron  $i$  is given by  $W_{ij}$ , and  $I_i$  is the input current to neuron  $i$ . When the connectivity is constrained to be symmetric,  $W = W^\top$ , we introduce the *energy potential*,

$$E(\mathbf{v}) = -\frac{1}{2} \sum_{j,i} W_{ij} v_i v_j - \sum_i I_i v_i + \sum_i \int_0^{v_i} h^{-1}(\omega) d\omega, \quad (3)$$

and  $\tilde{E}(\mathbf{u}) = E(\mathbf{h}(\mathbf{u}))$ . The drift can be written in the form,

$$\mathbf{F}(\mathbf{u}) = -\nabla_{\mathbf{v}} E(\mathbf{v}), \quad (4)$$

$$= -\mathbf{D}(\mathbf{u}) \nabla_{\mathbf{u}} \tilde{E}(\mathbf{u}), \quad (5)$$

where  $\mathbf{D}(\mathbf{u}) = \text{diag}\left(\frac{1}{h'(u_1)}, \dots, \frac{1}{h'(u_n)}\right)$  is a positive-definite matrix-valued function. As a result, the RNN is constrained to perform ‘generalised’ gradient descent on the energy landscape, eventually arriving at an energy minimum.<sup>1</sup> Hopfield’s model allows for the manipulation of the energy landscape via training, such that a desired ‘memory’ can be encoded as an energy minimum. The result is an autonomous neural circuit that will ‘retrieve the memory given initial information’ i.e. converge to the energy minimum from an appropriate initial state. Hopfield’s results laid the ground work for the study of *attractor neural networks*, and their possible implications for neuroscience [13, 14].

<sup>1</sup>The prefactor  $\mathbf{D}(\mathbf{u})$  causes the gradient to be scaled unevenly in different directions, thus the system does not follow the Euclidean direction of steepest descent on the landscape. Instead, the drift is a gradient flow with respect to the Riemannian metric defined by  $\mathbf{D}(\mathbf{u})^{-1}$ . Practically, we would see that the system descends the landscape monotonically, but more quickly in directions where  $h'(u_i)$  is small.

Despite Hopfield's application to associative memory, limiting to symmetric connectivity severely constrains the repertoire of dynamics within the system, precluding the existence of limit-cycles and other dynamic phenomena. Moreover, asymmetry is ubiquitous in biological neural circuits, thus the symmetric assumption limits the neuroscientific plausibility of such a model. Numerous studies have analysed asymmetric Hopfield networks, but these typically consider the discrete, spin-glass form of the model [15–17], and analyse the attracting states emerging from random connectivity. On the other hand, in the continuous model, asymmetric connectivity disrupts the energy landscape eroding the ability of the network to preserve attracting states [18]. Moreover, the dichotomy of symmetric and asymmetric connectivity is closely related to the necessary departure from equilibrium to nonequilibrium statistical mechanics, which has become an emerging area of research in neuroscience, neural computation, and associative memory [18–24].<sup>2</sup>

In an entirely separate development, dimensionality reduction techniques have shown the emergence of low-dimensional, latent structure in high-dimensional neural activity associated with tasks like motor control, navigation and working memory [25, 26]. These so-called *neural manifolds* indicate that high-dimensional brain network activity is, in fact, constrained to low-dimensional subspaces where the dynamics are often more mechanistically interpretable. These low-dimensional dynamics are responsible for computation and may also emerge in RNNs [27], typically associated with *low-rank* structure in the connectivity [28, 29]. Neural manifolds are just a single example forming part of the more general hypothesis that real-world network dynamics are effectively low-dimensional [30, 31], which in turn can be seen as a special case of the well-known *manifold hypothesis* for high-dimensional data [32]. Neural data analysis has provided significant evidence that computational dynamics are encoded at the level of latent manifolds in empirical brain network activity [25, 26, 33]. As a result, understanding how such cognitive processes can be encoded in RNNs via neural manifolds is crucial to understanding the mechanisms and limits of neural computation.

In this article, we fuse together asymmetric attractor neural networks with the theory of neural manifolds by proposing the *drift-diffusion matching* framework to train RNNs with the objective of representing any target SDE in a latent affine subspace (Fig. 1). As a result, we show that sufficiently large RNNs can encode arbitrary dynamics in this latent space, provided asymmetric connectivity is permitted, illustrating this by embedding nonlinear, and nonequilibrium systems, such as chaotic attractors, within the RNN. Next, to illustrate how the

theory can be linked to associative memory, we introduce two classes of SDEs, both of which have a number of attracting states. The first is the gradient of a tiltable energy potential, which allows the network to choose between energy minima using input-driven switching. The second is a nonequilibrium stationary diffusion that cycles autonomously between attractors in a specified order using irreversible currents. We present these as illustrative models of both input-driven associative and sequential (episodic) associative memory [34]. We apply our framework to show that such dynamics can be encoded in a latent subspace of an asymmetric RNN. In order to investigate how the dynamics are encoded in the network, we introduce two decompositions of an RNN, the first based on the asymmetry of the connectivity, and the second on the time-irreversibility of the RNN. This theoretical model suggests that populations of neurons with asymmetric connectivity are capable of encoding a wide array of dynamical systems, including attractor-switching and -cycling dynamics, thus extending Hopfield's model and integrating it with the theory of neural manifolds.

## II. RECURRENT NEURAL NETWORKS WITH TARGET LATENT DYNAMICS

### A. Drift-diffusion matching

We focus once more on the RNN of the form,

$$\begin{aligned} d\mathbf{u}(t) &= \mathbf{F}(\mathbf{u}) dt + B d\mathbf{w}(t), \\ F_i &= -u_i + \sum_j W_{ij} v_j + I_i, \end{aligned} \quad (6)$$

for  $i = 1, \dots, n$ , and consider a latent *affine subspace*  $\mathcal{A} = \{\mathbf{u} \in \mathbb{R}^n : \mathbf{u} = \Gamma \mathbf{y} + \mathbf{b}, \mathbf{y} \in \mathbb{R}^k\}$  for some  $\Gamma \in \mathbb{R}^{n \times k}$  and  $\mathbf{b} \in \mathbb{R}^n$  for some latent dimension  $k \ll n$ . We first ask if  $\{W, I, B, \Gamma, \mathbf{b}\}$  can be chosen such that the dynamics of our latent parametrisation,  $\mathbf{y}(t)$ , follow a target SDE of the form,

$$d\mathbf{y}(t) = \mathbf{f}(\mathbf{y}) dt + \sigma d\mathbf{w}(t), \quad (7)$$

where  $\mathbf{f}$  is the drift of the target process, and  $\sigma d\mathbf{w}(t)$  is isotropic noise in  $\mathbb{R}^k$ .

A variety of methods exist to train RNNs. For systems with feedback, such as reservoir computers, approaches include 'echo-state' [35], 'FORCE' learning [5], direct programming [8], and the 'Neural Engineering Framework' [36]. For sequence learning from data, models are trained through *back-propagation through time* (BPTT) [37], a training procedure that is computationally expensive, especially for stochastic data, and numerically unstable, often suffering from vanishing and exploding gradients [38]. Instead, we opt to train our RNNs using, what we denote as, *drift-diffusion matching* (DDM), where we directly align the drift and diffusive terms in the affine subspace to the target SDE. Firstly, we assume that  $\Gamma$  has full rank  $k$ , thus it has a Moore-Penrose (MP) inverse such that  $\Gamma^\dagger \Gamma = \mathbf{I}_k$ , where  $\mathbf{I}_k$  is the identity in  $\mathbb{R}^k$ . Using Ito's rule [12], we have that the drift in the affine subspace is

<sup>2</sup>It is worth noting that Hopfield's discrete, stochastic model [10] is equivalent to a symmetric Ising model, and therefore is in thermodynamic equilibrium [23]. Turning to the continuous model [11], we note that whilst gradient-flow dynamics are reversible [12], this model is only a gradient flow in the appropriate Riemannian metric, thus does not preserve detailed balance in Euclidean space. Nevertheless, it is constrained to descend an energy function and cannot admit rich, time-dependent, nonequilibrium behaviour without asymmetry.

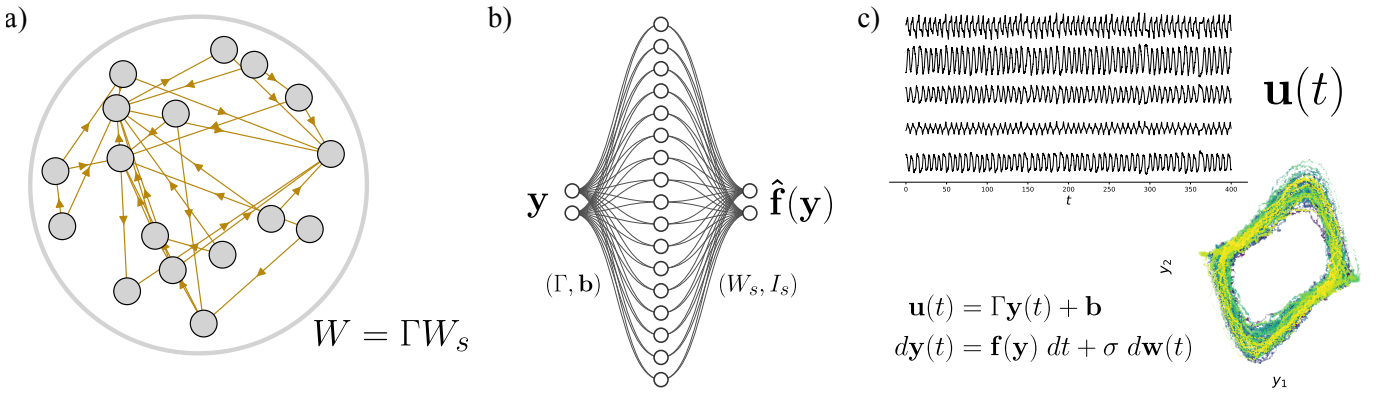


FIG. 1. **Embedding dynamics in latent manifolds of RNNs.** *a)* Our framework focuses on RNNs with low-rank connectivity of the form  $W = \Gamma W_s$ , where  $\Gamma \in \mathbb{R}^{n \times k}$  with  $k \ll n$ . We train these autonomous systems to encode arbitrary stochastic dynamics in a learnt affine subspace. *b)* The training of the RNN can be reformulated as the training of a two-layer perceptron to approximate a target vector field. *c)* Once the parameters of the RNN have been fitted, it can be integrated over time as an autonomous circuit which produces stochastic dynamics. Here we plot traces from 5 of 64 neurons in a network trained to approximate the van der Pol oscillator. When we project the dynamics into the learnt subspace, we recover a trajectory from the stochastic van der Pol system, which has been embedded into the RNN.

given by,

$$\hat{\mathbf{f}}(\mathbf{y}) = \Gamma^\dagger (\mathbf{F}(\Gamma \mathbf{y} + \mathbf{b})), \quad (8)$$

whilst the diffusion matrix is,

$$\Sigma = \Gamma^\dagger B B^\top (\Gamma^\dagger)^\top. \quad (9)$$

However, matching  $\hat{\mathbf{f}} = \mathbf{f}$  and  $\Sigma = \sigma^2 \mathbf{I}_k$ , is not sufficient to guarantee that projections of trajectories from the RNN, will behave as trajectories from the target SDE. This is due to the presence of the drift and diffusion terms in directions orthogonal to the affine subspace. To guarantee that DDM enforces that projections of the RNN trajectory recover trajectories from the target SDE, we must ensure there is a one-to-one relationship between the latent point  $\mathbf{y}(t)$  and the high-dimensional  $\mathbf{u}(t)$ . Each point in the trajectory can be uniquely decomposed as,

$$\mathbf{u}(t) = \mathbf{u}_{\parallel}(t) + \mathbf{u}_{\perp}(t), \quad (10)$$

where  $\mathbf{u}_{\parallel} = \Gamma \mathbf{y} + \mathbf{b} \in \mathcal{A}$ , whilst  $\mathbf{u}_{\perp} \perp \text{Im}(\Gamma)$  i.e.  $\mathbf{u}_{\perp}$  is orthogonal to the image of  $\Gamma$ . As a result,  $\Gamma^\dagger(\mathbf{u} - \mathbf{b}) = \mathbf{y}$  for all different  $\mathbf{u}_{\perp} \perp \text{Im}(\Gamma)$ , thus it is not injective.

To prevent dynamics in directions that are not ‘visible’ under the projection, we enforce a low-rank parametrisation of the RNN,

$$W = \Gamma W_s, \quad I = \Gamma I_s + \mathbf{b}, \quad B = \Gamma B_s, \quad (11)$$

where  $W_s \in \mathbb{R}^{k \times n}$ ,  $I_s \in \mathbb{R}^k$ ,  $B_s \in \mathbb{R}^{k \times d}$ , where we recall that  $d$  is the number of independent noise sources. The result of this parameterisation is that, for any  $\mathbf{u} \in \mathcal{A}$ , we have that,

$$\mathbf{F}(\mathbf{u}) = -\mathbf{u} + \Gamma W_s \mathbf{h}(\mathbf{u}) + \Gamma I_s + \mathbf{b} \in \text{Im}(\Gamma), \quad (12)$$

where  $\mathbf{h}(\mathbf{u}) = (h(u_1), \dots, h(u_n))$ . Moreover, we have that  $\Gamma B_s d\mathbf{w}(t) \in \text{Im}(\Gamma)$ . Together, these imply that, given  $\mathbf{u}(0) \in$

$\mathcal{A}$ , the drift and diffusion are tangent to the subspace, and thus  $\mathbf{u}(t) \in \mathcal{A}$  for all  $t > 0$  i.e the dynamics are constrained to the affine subspace. When the process begins outside the subspace, the ‘leak term’,  $-\mathbf{u}$ , will cause the process to drift to the origin along the directions orthogonal to  $\text{Im}(\Gamma)$ .

Under this parametrisation, the dynamics in the affine subspace simplify significantly,

$$\hat{\mathbf{f}}(\mathbf{y}) + \mathbf{y} = W_s \mathbf{h}(\Gamma \mathbf{y} + \mathbf{b}) + I_s, \quad (13)$$

where we have moved the leak term to the left-hand-side for convenience. Here, we can notice the right-hand-side is equivalent to a two-layer perceptron with a  $k$ -neuron input layer, a  $n$ -neuron hidden layer, and a  $k$ -neuron output layer (Fig. 1b)). The input-to-hidden weights and biases are given by  $\Gamma$  and  $\mathbf{b}$  respectively, whilst the hidden-to-output weights and biases are given by  $W_s$  and  $I_s$ , and where  $\mathbf{h}(\cdot)$  plays the role of the element-wise activation function. It is well-known that this parametrisation is a *universal approximator* i.e. it can approximate any continuous function to arbitrary accuracy [39]. Moreover, it can be efficiently optimised via backpropagation of error [40]. The diffusion matrix in the affine subspace also simplifies to  $B_s B_s^\top$ .

Given this insight, we can setup the DDM loss function to be,

$$\begin{aligned} \mathcal{L}_{\text{DDM}} = & \|\mathbf{f}(\mathbf{y}) + \mathbf{y} - W_s \mathbf{h}(\Gamma \mathbf{y} + \mathbf{b}) - I_s\| \\ & + \lambda_{\text{diff}} \|\sigma^2 \mathbf{I}_k - B_s B_s^\top\|, \end{aligned} \quad (14)$$

where  $\lambda_{\text{diff}}$  is a hyper-parameter controlling the relative importance of the drift and diffusion losses, and where we optimise over the parameters  $\{\Gamma, \mathbf{b}, W_s, I_s, B_s\}$ , for a total of  $2nk + n + k + kd$  free parameters.

## B. Latent dynamics of symmetric networks

Previously, we noted that the drift of an RNN with symmetric connectivity can be written in the form,

$$\mathbf{F}(\mathbf{u}) = -\mathbf{D}(\mathbf{u})\nabla_{\mathbf{u}}\tilde{E}(\mathbf{u}),$$

i.e. as a generalised gradient flow that monotonically descends the energy landscape, defined in Eq. (3), to a local minimum. Now we focus on the case of a low-rank, but symmetric network projected onto the affine subspace,  $\mathcal{A}$ , given the parametrisation in Eq. (11).

We define an additional energy function on  $\mathcal{A}$ ,  $S(\mathbf{y}) = \tilde{E}(\Gamma\mathbf{y} + \mathbf{b})$  whose gradient is therefore  $\nabla_{\mathbf{y}}S(\mathbf{y}) = \Gamma^{\top}\nabla_{\mathbf{u}}\tilde{E}(\Gamma\mathbf{y} + \mathbf{b})$ . The dynamics in the affine subspace are given by,

$$\begin{aligned}\hat{\mathbf{f}}(\mathbf{y}) &= -\Gamma^{\dagger}\mathbf{D}(\Gamma\mathbf{y} + \mathbf{b})(\Gamma^{\dagger})^{\top}\nabla_{\mathbf{y}}S(\mathbf{y}), \\ &= -\mathbf{K}(\mathbf{y})\nabla_{\mathbf{y}}S(\mathbf{y}),\end{aligned}\quad (15)$$

where  $\mathbf{K}(\mathbf{y})$  is positive definite i.e. the dynamics in  $\mathcal{A}$  also admit an energy function. As a result, a symmetric RNN induces an energy potential over the subspace, and precludes limit-cycles or chaotic attractors. Therefore, any dynamics which go beyond monotonic decreases in energy must be encoded via the asymmetry of the connectivity matrix.

## C. Symmetric-asymmetric decomposition of neural network dynamics

The observations made in the previous section, that the projected dynamics of a symmetric RNN remain a generalised gradient flow, motivate a decomposition of a trained RNN into a symmetric and asymmetric component. We consider  $W = W_{\text{sym}} + W_{\text{asym}}$ , where the symmetric component,  $W_{\text{sym}}$ , descends an energy landscape, whilst the asymmetric component,  $W_{\text{asym}}$ , encodes rotational dynamics,

$$\begin{aligned}\hat{\mathbf{f}} &= \hat{\mathbf{f}}_{\text{sym}} + \hat{\mathbf{f}}_{\text{asym}}, \\ \hat{\mathbf{f}}_{\text{sym}}(\mathbf{u}) &= -\mathbf{u} + W_{\text{sym}}\mathbf{h}(\mathbf{u}) + I, \\ \hat{\mathbf{f}}_{\text{asym}}(\mathbf{u}) &= W_{\text{asym}}\mathbf{h}(\mathbf{u}).\end{aligned}\quad (16)$$

This decomposition has similarities to the Helmholtz-Hodge decomposition of a vector field [41] or SDE [42], or the GENERIC decomposition of a stochastic process [43]. However, it is not identical to either, as the symmetric component is neither a conservative field, nor is it equal to the time-reversible component of the stochastic process. We consider decompositions based on time-irreversibility in more detail in Sec. III and IV.

At first glance, it is natural to use the unique decomposition of the network into a symmetric and antisymmetric component,

$$W = \frac{1}{2}(W + W^{\top}) + \frac{1}{2}(W - W^{\top}), \quad (17)$$

where antisymmetric means  $A = -A^{\top}$ . However, with this decomposition, the drift components,  $\hat{\mathbf{f}}_{\text{sym}}$  and  $\hat{\mathbf{f}}_{\text{asym}}$ , are no

longer confined to the affine subspace. As a result, whilst the symmetric network will still admit an energy function on  $\mathbb{R}^n$ , for the projected dynamics to follow an energy function,  $S(\mathbf{y})$ , on  $\mathbb{R}^k$  requires that  $W_{\text{sym}} = \Gamma A$  for some  $A$ , which is not necessarily true, even if  $W = \Gamma W_s$ . Thus the projected dynamics of this symmetric component of the network are not ‘attractor’-like and, in general, the process does not converge to the minimum of the projected energy function  $S(\mathbf{y})$ .

To tackle this problem, we introduce a more motivated decomposition given the low-rank structure of the network. We split the network as,

$$W = \Gamma(\Omega + \Pi), \quad (18)$$

where  $\Gamma\Omega = (\Gamma\Omega)^{\top}$  i.e. it is symmetric. Let us note that  $\Gamma\Pi$  is asymmetric, unless  $W = W^{\top}$ , but not antisymmetric, except in the special case when this decomposition coincides with Eq. (17). Such a decomposition is clearly not unique, thus we define the ‘best’ decomposition to be,

$$\Omega = \operatorname{argmin}_{A \in \mathbb{R}^{k \times n}} \|\Gamma A - C\|_F^2, \quad (19)$$

where  $C = \frac{1}{2}(W + W^{\top})$  i.e. our symmetric part is the most similar to the canonical decomposition, with respect to the Frobenius norm. This problem has a closed form solution (see App. B),

$$\Omega = \Gamma^{\dagger}C\Gamma\Gamma^{\dagger}. \quad (20)$$

This ‘improved’ decomposition gives two drift components, where both are constrained to the affine subspace, and where  $\hat{\mathbf{f}}_{\text{sym}}$  descends the energy function  $S(\mathbf{y})$  associated with the network  $W_{\text{sym}} = \Gamma\Omega$ .

## D. Pipeline and examples

To illustrate the DDM framework and the network decomposition, we first consider three well-known nonlinear systems with additive noise. We train an RNN with 64, 512, and 1024 neurons for each of the systems respectively, using the DDM framework. Using the fitted parameters, we integrate the RNN as an autonomous SDE using the Euler-Maruyama scheme (see App. A 1). Projecting the dynamics into the learnt affine subspace, we recover trajectories from the target SDE. Next, we decompose the RNN connectivity as described in Sec. II C, where we can investigate which features of the dynamics are encoded in each part of the network respectively. The examples we consider include:

- The stochastic *van der Pol* (VDP) oscillator is a nonlinear, planar system with a stable limit cycle. It is given by the system,

$$d \begin{pmatrix} y_1(t) \\ y_2(t) \end{pmatrix} = \begin{pmatrix} y_2 \\ -y_1 + \mu y_2(1 - y_1^2) \end{pmatrix} dt + \sigma d \begin{pmatrix} w_1(t) \\ w_2(t) \end{pmatrix}, \quad (21)$$

where we take  $\mu = 1$  [44].

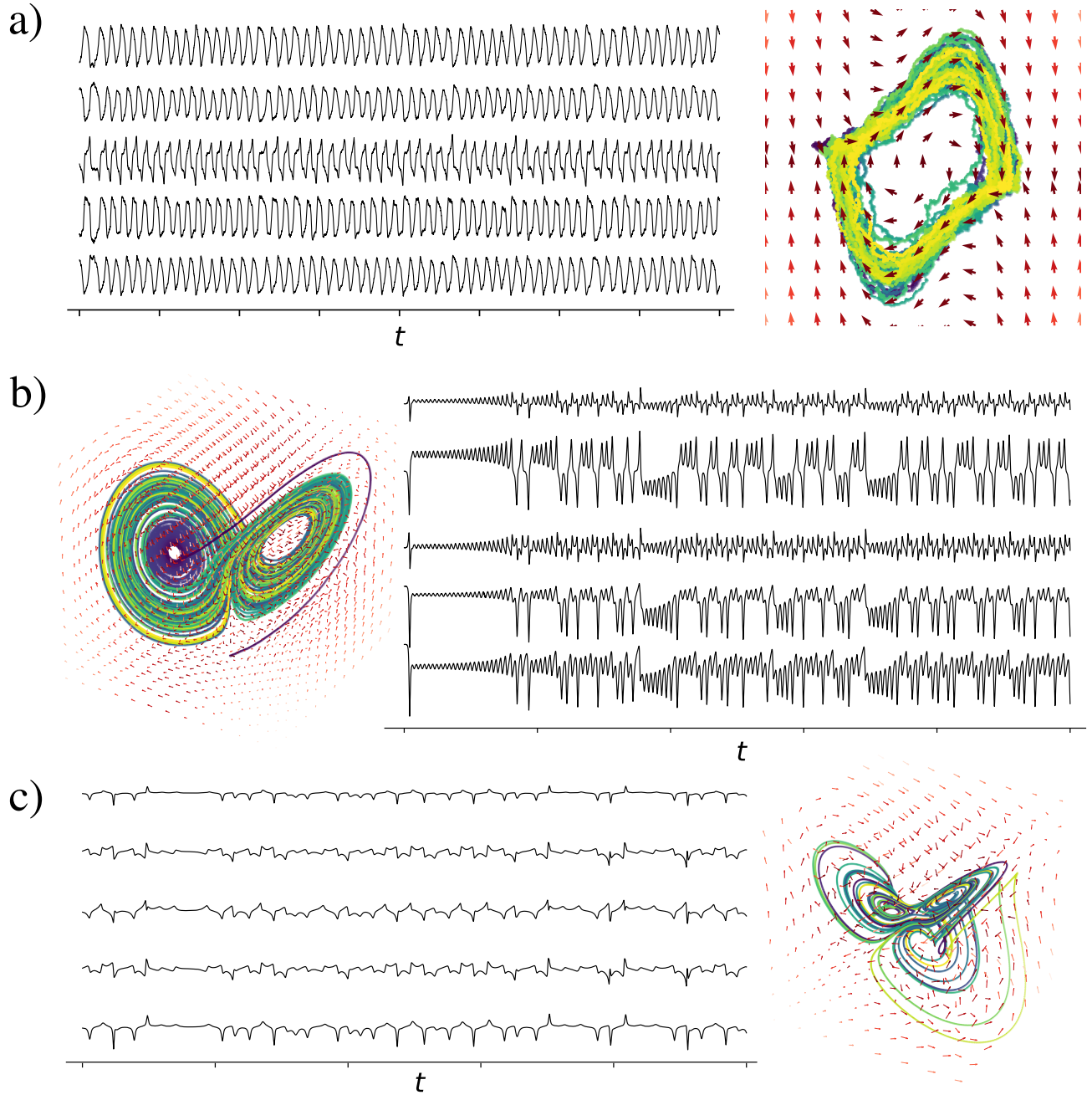


**FIG. 2. Embedding attractors in neural networks.** *a)* Traces from 5 randomly selected neurons in a 64-neuron RNN trained to embed a stochastic VDP oscillator in a latent subspace. In the subspace, we see the characteristic VDP limit-cycle. *b – c)* Traces from a 512-neuron RNN trained to embed the LA, and a 1024-neuron RNN trained to embed the DA.

- The stochastic *Lorenz attractor* (LA) is a three-dimensional chaotic system given by,

$$d \begin{pmatrix} y_1(t) \\ y_2(t) \\ y_3(t) \end{pmatrix} = \begin{pmatrix} \zeta(y_2 - y_1) \\ y_1(\rho - y_3) - y_2 \\ y_1y_2 - \beta y_3 \end{pmatrix} dt + \sigma d \begin{pmatrix} w_1(t) \\ w_2(t) \\ w_3(t) \end{pmatrix}. \quad (22)$$

The system has a characteristic strange attractor with two scrolls when  $\zeta = 10$ ,  $\rho = 28$ , and  $\beta = 8/3$  [44].

- The stochastic *Dadras attractor* (DA) is a three-

dimensional chaotic system given by,

$$d \begin{pmatrix} y_1(t) \\ y_2(t) \\ y_3(t) \end{pmatrix} = \begin{pmatrix} y_2 - py_1 + oy_2y_3 \\ ry_2 - y_1y_3 + y_3 \\ cy_1y_2 - ey_3 \end{pmatrix} dt + \sigma d \begin{pmatrix} w_1(t) \\ w_2(t) \\ w_3(t) \end{pmatrix}. \quad (23)$$

The system has a strange attractor with three scrolls when  $p = 3$ ,  $o = 2.7$ ,  $r = 1.7$ ,  $c = 2$ , and  $e = 9$  [45].

Fig. 2 shows example traces from 5 randomly selected neu-

rons in each of the RNNs, alongside the phase-plane dynamics in the learnt latent space. We see that the system is able to encode all three nonlinear systems, and that the trajectories of individual neurons mirror the qualities of the embedded attractor.

Fig. 3 shows the results of the decomposition for the VDP, LA, and DA examples. This decomposition gives us two vector field components, one of which has an associated energy function. Panels *a* – *c*) show both components for each system, whilst Panels *d* – *e*) show characteristic isopotentials of the energy function for the LA and DA systems. It appears that for the VDP and DA systems, the symmetric component of the network encodes attracting dynamics that maintain the process near the attractor, whilst the asymmetric component drives nonlinear rotation in phase-space. On the other hand, for the LA, the energy gradient appears to drive the process away from the origin, with the asymmetric, rotational component preventing it from diverging.

### E. Reconstructing affine subspaces from trajectories

Another pertinent question is whether or not we can reconstruct the appropriate affine subspace given only trajectories from the RNN. Given dynamics that are entirely constrained to an affine subspace, it is possible to exactly identify the subspace, up to numerical accuracy. The solution comes from a seminal result by Pearson, and is known as *principal component analysis* (PCA) [46]. Additionally, if the trajectory data has measurement error or noise in the form of isotropic Gaussian variation in the directions orthogonal to the subspace, then it is not entirely constrained and an exact recovery is not possible, but PCA becomes the maximum-likelihood estimator of the subspace. Subspace identification through PCA is extremely common in the analysis of neural data, and has been used in countless studies to identify neural manifolds in brain network activity [33, 47, 48], as well as to identify latent subspaces in the activity of trained RNNs [27, 49].

This method is canonical and the proofs have been reviewed at length (e.g. [50]), thus we will only outline the approach in brief, and illustrate how it applies to our setting. Given trajectory data of the form  $\{\mathbf{u}(t_j) : j = 1, \dots, T\}$ , we assume the data lives in an affine subspace of dimension  $k$ , where  $k$  typically begins as an unknown, and can be written in the form,

$$\mathbf{u} = \Psi \mathbf{v} + \boldsymbol{\mu}, \quad (24)$$

where  $\Psi \in \mathbb{R}^{n \times k}$  has orthonormal columns,  $\boldsymbol{\mu} \in \mathbb{R}^n$ , and  $\mathbf{v}(t) \in \mathbb{R}^k$  is a parametrisation.

Whilst it is tempting to associate  $\Psi$  with  $\Gamma$  and  $\boldsymbol{\mu}$  with  $\mathbf{b}$ , we note that this is not necessarily the case. Whilst the subspace can be identified, the exact parametrisation cannot be, as for any invertible matrix  $A$ , we have indistinguishable parametrisations,  $\mathbf{u} = \Gamma \mathbf{y} + \mathbf{b} = (\Gamma A^{-1})(A \mathbf{y}) + \mathbf{b} = \tilde{\Gamma} \tilde{\mathbf{y}} + \mathbf{b}$ . Moreover, our parameterisation could be shifted arbitrarily,  $\mathbf{u} = \Gamma(\mathbf{y} - \mathbf{c}) + \mathbf{b} + \Gamma \mathbf{c}$ . Thus, the parametrisation we obtain is equivalent to the original parametrisation, up to an affine transformation.

We stack our time-series into the matrix  $\mathbf{U} \in \mathbb{R}^{n \times T}$  and center it,  $\mathbf{X} = \mathbf{U} - \bar{\mathbf{u}}$ , where

$$\bar{\mathbf{u}} = \frac{1}{T} \left( \sum_j u_1(t_j), \dots, \sum_j u_n(t_j) \right). \quad (25)$$

This is equivalent to choosing  $\boldsymbol{\mu} = \mathbf{0}$ . Next, we take the singular value decomposition (SVD) of  $\mathbf{X}$ . For long trajectories, it is more efficient to compute the covariance matrix,  $\Theta = \mathbf{X} \mathbf{X}^\top$ , and compute its eigendecomposition. Assuming that the dynamics are exactly constrained to the subspace, then this matrix will have  $k$  non-zero eigenvalues, whose eigenvectors form the columns of  $\Psi$ , which we call *principal components* (PCs), and where we order the columns by decreasing eigenvalue magnitude,  $\{\lambda_1, \dots, \lambda_k\}$  and  $\lambda_j = 0$  for  $j \in \{k+1, \dots, n\}$ . The zero eigenvalues correspond to the directions orthogonal to the subspace, in which the dynamics do not evolve. For noisy data, these eigenvalues are non-zero but very small. In this case, the dimension of the subspace,  $k$ , can be approximately identified by considering the *proportion of the variance explained* by each PC,  $\vartheta_l = \lambda_l / \sum_{j=1}^n \lambda_j$ , where we ‘cut-off’ after  $k$  components, if  $\sum_{j=1}^k \vartheta_j > c$ , where  $c$  is a threshold e.g.  $c = 0.7$  [50]. We then project the time-series to obtain the parameterisation,  $\mathbf{v} = \Psi^\top \mathbf{X}$ . Panels *a* – *b*) of Fig. 4 show the traces and phase-space dynamics of the 3 non-trivial PCs for a trajectory from the 512-neuron RNN trained to embed the LA.

Given  $\Gamma$  and  $\mathbf{b}$ , we can find the affine transformation that turns  $\mathbf{v}(t)$  to  $\mathbf{y}(t)$ . We can solve  $\Gamma \mathbf{v} = \Psi$  and  $\Gamma \mathbf{v} = \bar{\mathbf{u}} + \mathbf{b}$  as a least-squares problem, and apply the transformation  $\mathbf{y}(t) = \mathbf{v}(t) + \mathbf{b}$ , to obtain the original parametrisation, as shown in Panel *c*) of Fig. 4.

## III. SWITCHING AND CYCLING BETWEEN ATTRACTORS

Attractor dynamics are frequently cited as both emergent features in neural data, and as a possible mechanism for computation via dynamics [13, 14]. These attractors are most easily understood in terms of energy landscapes, where the dynamics perform some kind of gradient descent, arriving at a local minima in the form of a fixed point or other low-dimensional manifold e.g. a line or a ring. On the one hand, a range of computational mechanisms, both neuroscientific and other, rely on such dynamics, including stochastic gradient descent [40], the ‘free-energy’ principle [51], and the class of so-called energy-based models [52]. On the other hand, in both neural and biological systems, asymmetry and non-reciprocity are ubiquitous, typically disrupting the dynamics associated with symmetric models and their energy landscapes [18, 19, 53–55]. However, designing learning systems that utilise such dynamics has, so far, been evasive.

Based on our method to train an asymmetric RNN to encode an arbitrary system in a latent affine subspace, we now introduce two classes of SDEs that are defined by energy potential gradients and thus have attracting dynamics. The first of these uses network inputs to *switch* between the minima

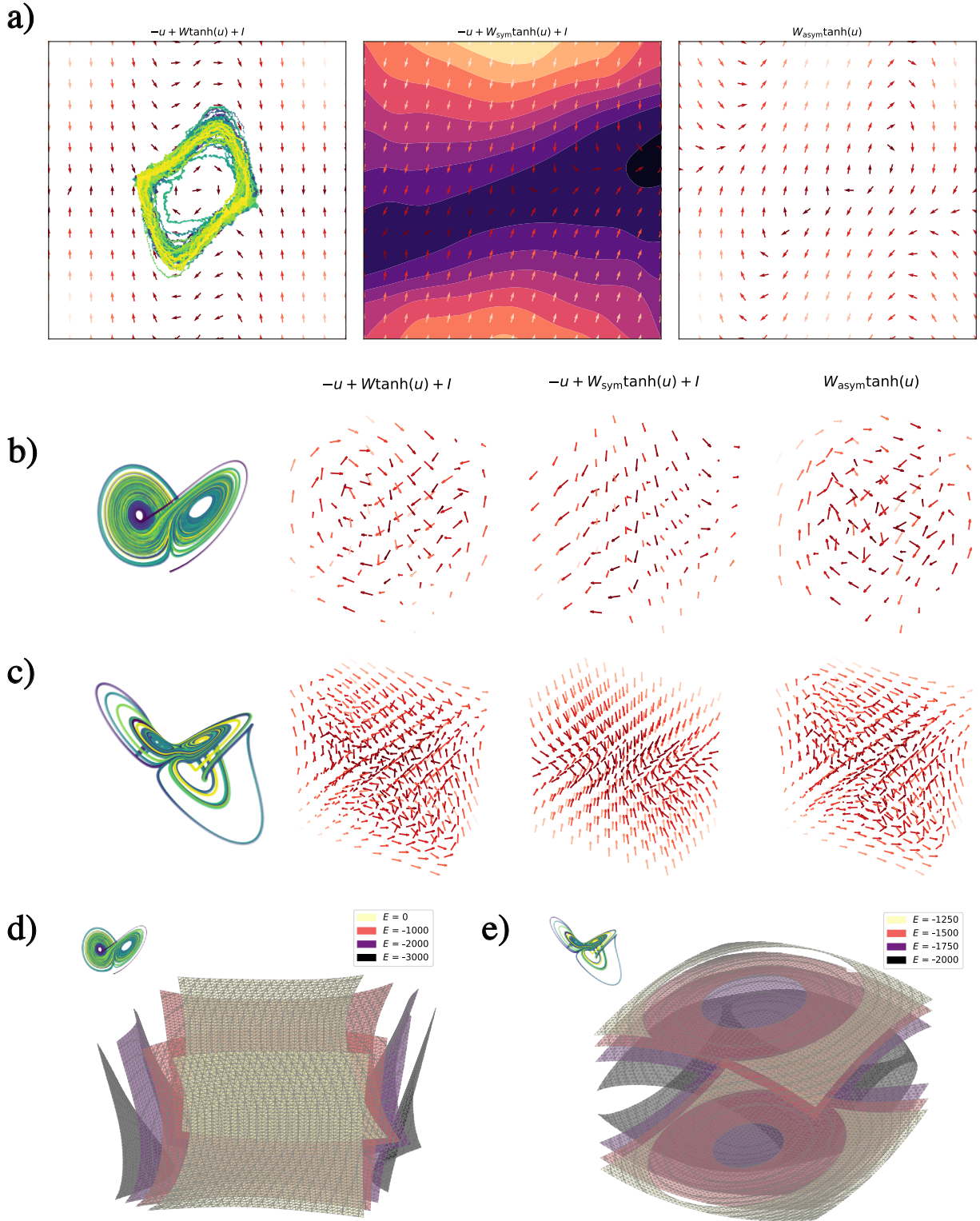


**FIG. 3. Symmetric-asymmetric decomposition of RNNs.** *a)* Decomposition of RNN trained to encode the VDP. The symmetric dynamics descend the contoured energy function. This appears to keep the process near the limit cycle, whilst the asymmetric component provides rotational dynamics. *b – c)* Decompositions of RNNs trained to encode the LA and DA. For the DA, the symmetric dynamics keep the process near the attractor, whilst the asymmetric component provides rotational dynamics. For the LA, it appears the symmetric component pushes the dynamics away from the origin, and the asymmetric component provides a restoring force. *d – e)* This is confirmed by plotting isopotentials of the energy functions for the LA and DA respectively.

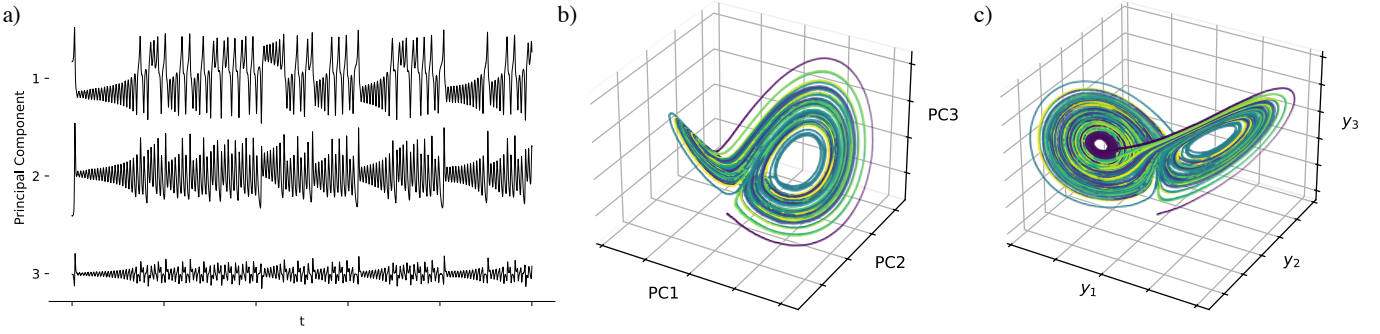


**FIG. 4. Reconstructing latent subspaces from trajectories.** *a)* Trajectories from a low-rank RNN trained to embed a  $k$ -dimensional system only have  $k$  non-zero principal components. *b)* With PCA, we can identify the affine subspace in which the dynamics are constrained. *c)* The PCA representation is equivalent to original coordinates up to an affine linear transformation. Given  $(\Gamma, \mathbf{b})$  can solve for this transformation to recover the original coordinates.

of the energy potential. Here the network inputs represent sensory information or the output of a disjoint neural circuit, which prompts the RNN to retrieve a particular memory in light of this information. This is a more complex extension of Hopfield’s model, where the initial network state serves as the input, and the system cannot transition between memories. The second is a class of stationary diffusions that use irreversible, rotational currents to cycle between minima in a preferred direction. In this case, our model attempts to describe the ability of a memory system to autonomously transition between a series of a related memories in a preferred direction. We show that both these dynamics can be encoded within an RNN, as illustrative examples of how a neural circuit could encode more complex forms of associative memory.

Before progressing, we introduce some preliminaries for stochastic dynamics and their nonequilibrium steady-states. The general form for SDEs which we will consider is given by,

$$d\mathbf{y}(t) = \mathbf{f}(\mathbf{y}) dt + \Sigma d\mathbf{w}(t), \quad (26)$$

with  $\mathbf{y}(t) \in \mathbb{R}^k$  and  $\Sigma \in \mathbb{R}^{k \times d}$ . The diffusion matrix is defined by  $D = \Sigma \Sigma^\top / 2$  which is positive semidefinite. We will focus on cases where the drift  $\mathbf{f}$  is designed to encode descent of an energy landscape and, in the second case, an additional rotational flow between minima. The *Fokker-Planck* (FP) equation describes the dynamics of the probability density,  $p(\mathbf{y}, t)$ ,

$$\begin{aligned} \partial_t p &= -\nabla \cdot \mathbf{J}, \\ \mathbf{J}(\mathbf{y}, t) &= \mathbf{f}(\mathbf{y})p(\mathbf{y}, t) - D\nabla p(\mathbf{y}, t), \end{aligned} \quad (27)$$

where  $\mathbf{J}$  is the probability flux [12]. The SDE is ergodic with stationary density  $\pi(\mathbf{y})$  if  $p(\mathbf{y}, t) \rightarrow_{t \rightarrow \infty} \pi(\mathbf{y})$  and  $\nabla \cdot \mathbf{J}_{ss} = 0$ , where  $\mathbf{J}_{ss}$  is the flux with respect to the density  $\pi$ .

A stationary process is said to be an *equilibrium steady-state* (ESS) if  $\mathbf{J}_{ss} = 0$ , which is also known as the *detailed balance condition*, and implies that the process is time-reversible [56]. Otherwise, the process is in a *nonequilibrium steady-state* (NESS), is time-irreversible, and produces entropy. We also introduce the *Helmholtz-Hodge decomposition* (HHD) of the process, which decomposes the drift of a stationary diffu-

sion into two components,

$$\mathbf{f} = \mathbf{f}_{\text{rev}} + \mathbf{f}_{\text{irr}}, \quad \mathbf{f}_{\text{rev}} = D\nabla \log \pi, \quad \mathbf{f}_{\text{irr}} = \mathbf{J}_{ss}/\pi, \quad (28)$$

where  $\mathbf{f}_{\text{rev}}$  is a time-reversible (shifted) gradient flow and  $\mathbf{f}_{\text{irr}}$  is the time-irreversible circulation [42]. Finally, the degree of irreversibility can be quantified by the *entropy production rate* (EPR), given by,

$$\Phi = \int_{\mathbb{R}^k} (\mathbf{f}_{\text{irr}})^\top D^{-1} \mathbf{f}_{\text{irr}} \pi d\mathbf{y}, \quad (29)$$

which is non-negative, and zero if and only if the process is in detailed balance [56].<sup>3</sup>

### A. Input-driven attractor-switching

We consider an RNN of the form,

$$\begin{aligned} d\mathbf{u}(t) &= \mathbf{F}(\mathbf{u}) + G\mathbf{s}(t) dt + B d\mathbf{w}(t), \\ F_i &= -u_i + \sum_j W_{ij} v_j + I_i, \end{aligned} \quad (30)$$

where we have an additional *input* term  $G\mathbf{s}(t) + \Gamma\mathbf{d}$ , where  $\mathbf{s}(t) \in \mathbb{R}^l$  is the low-dimensional input signal, and  $G \in \mathbb{R}^{n \times l}$  represents its projection into the RNN. The additional bias term,  $\Gamma\mathbf{d}$ , is low-rank and is absorbed into the input current  $I$  of the original RNN. Moreover, we assume that our input connectivity is also low-rank and of the form  $G = \Gamma G_s$ . As a result, the dynamics remain constrained to the affine subspace.

Next, we assume that our network, in the absence of inputs, encodes a gradient flow on an energy potential,  $V : \mathbb{R}^k \rightarrow \mathbb{R}$ , with a number of minima of approximately equal energy, and isotropic noise,

$$d\mathbf{y}(t) = -\nabla V(\mathbf{y}) dt + \sigma d\mathbf{w}(t). \quad (31)$$

<sup>3</sup>When  $D$  is not full-rank, we can use its MP inverse, provided certain conditions are met (see App. E and Ref. [42]).



FIG. 5. ‘Tilting’ the energy landscape. Our approach uses network inputs to ‘tilt’ the energy landscape, encouraging the process to push a trajectory into a particular energy minimum, by making it a global minimum. This is a soft version of the child’s ‘labyrinth’ game, where the board can be tilted such that the ball rolls into a specific hole – though in the actual game, one tries rather hard to avoid them.

Typically trajectories will be attracted to the closest minimum, eventually exploring the landscape via random diffusion. It is well-known that this process has a stationary *Boltzmann density*,

$$\pi(\mathbf{y}) = \frac{1}{Z} \exp\left(-\frac{2V(\mathbf{y})}{\sigma^2}\right), \quad (32)$$

and is in an ESS [12]. Our aim is to direct the system towards a particular minimum using the network input. The dynamics on the affine subspace can be written as,

$$d\mathbf{y}(t) = -\nabla V(\mathbf{y}) + G_s \mathbf{s}(t) + \mathbf{d} dt + \sigma d\mathbf{w}(t). \quad (33)$$

Considering a constant input over time, and defining  $\mathbf{c} = G_s \mathbf{s} + \mathbf{d}$ , we notice that the drift can be written as the gradient of a modified potential function,  $\mathbf{f}(\mathbf{y}) = -\nabla[V(\mathbf{y}) - \mathbf{c} \cdot \mathbf{y}]$ . Adding a term that is constant in  $\mathbf{y}$  corresponds to ‘tilting’ the potential to prioritise a particular minimum, making it a global minimum. This approach can be thought of in analogy with a child’s ‘labyrinth’ game (Fig. 5), where the objective is to tilt the board, which serves as the energy potential, such that the ball rolls into a particular hole i.e. the chosen energy minimum.

Assuming that the potential has a set of  $m$  deep, well-separated minima,  $\{\boldsymbol{\mu}_j\}_{j=1}^m$ , for each minima there is a convex subset  $\mathcal{C}_j \subset \mathbb{R}^k$ , where  $\mathbf{c} \in \mathcal{C}_j$  makes  $\boldsymbol{\mu}_j$  the global minimum. More explicitly, defining  $V_j^0 = V(\boldsymbol{\mu}_j)$ , if  $\mathbf{c} \cdot (\boldsymbol{\mu}_i^* - \boldsymbol{\mu}_j) > V_i^0 - V_j^0$  for all  $j \neq i^*$ , then  $\boldsymbol{\mu}_i^*$  is the global minimum, assuming the perturbation is small enough. Given values of  $\mathbf{c}$  for each minimum, it remains to compute  $(G_s, \mathbf{d})$  for a particular choice of coding scheme for the inputs. Example schemes include ‘one-hot’ or random Gaussian inputs. In App. A 2, we provide a concrete method for picking values of  $\mathbf{c}$  with quadratic programming, followed by computing an appropriate  $G_s$  and  $\mathbf{d}$  with ridge regression.

We now consider a numerical example. As the energy potential, we choose a sum of Gaussian wells,

$$V(\mathbf{y}) = - \sum_{j=1}^m a_j \exp\left(-\frac{\|\mathbf{y} - \boldsymbol{\mu}_j\|^2}{2v_j^2}\right), \quad (34)$$

where the  $m$  minima can be placed at arbitrary positions  $\boldsymbol{\mu}_j \in \mathbb{R}^k$ , and we can specify the depth,  $a_j$ , and breadth,  $v_j$ , of each well. As shown in Fig. 6, we place four identical minima at points in the plane. In the absense of inputs, the process typically converges to the minima that is closest. However, activating the corresponding input code, causes the potential to tilt and encourages trajectories to converge to a specified minimum. We train a 256-neuron RNN to encode the potential-gradient, then, using a one-hot coding for the inputs, we fit the input-connectivity and bias,  $G$  and  $\mathbf{d}$  (see App. A 2 for details). We then integrate the RNN with the input code for a given attractor, then switch it halfway through the trajectory. Panels b) and c) of Fig. 6 show traces of 10 random neurons in the network, and the projection of the network dynamics into the latent space, respectively. We see that the process converges to the first attractor, but then switches to the second due to the change in the input.

## B. Attractor-cycling stationary diffusions

In this section, we design a class of planar SDEs, which not only converge to energy minima, but also cycle between these minima in a preferred direction using irreversible currents. As before, we begin with an energy potential and define a gradient flow,

$$d\mathbf{y}(t) = -\nabla V(\mathbf{y}) dt + \sigma d\mathbf{w}(t). \quad (35)$$

In order to preserve the energy landscape, whilst adding in a rotational component, we consider a process of the form,

$$d\mathbf{y}(t) = -\nabla V(\mathbf{y}) + \mathbf{R}(\mathbf{y}) dt + \sigma d\mathbf{w}(t), \quad (36)$$

where we enforce that the process must still converge to the Boltzmann density. It is easy to show that the condition for this to be satisfied is that  $\nabla \cdot (\mathbf{R}\pi) = 0$  i.e. the rotational component is *divergence-free with respect to the stationary density* (DFSD). This condition is closely related to the HHD defined previously. In this case, we have simply that  $\mathbf{f}_{\text{rev}} = -\nabla V$  whilst  $\mathbf{f}_{\text{irr}} = \mathbf{R}$ . By adding on a rotational component that does not disrupt the Boltzmann density, we construct stationary diffusions that descend the energy landscape whilst being driven rotationally by stationary probability flux. In App. D, we construct both high-dimensional and non-coplanar examples. Specifically we design a process that can cycle between a pair of pixelated images in  $\mathbb{R}^{1024}$ , and another that cycles between minima placed on a saddle in  $\mathbb{R}^3$ , although we do not encode these in an RNN. We now focus on constructing planar examples, which we embed within an RNN.

In  $\mathbb{R}^2$ , or in the case that the attractors are coplanar in plane  $P$ , we can construct a differentiable, closed planar curve,  $\gamma$ , which connects points in the order that we would like the field

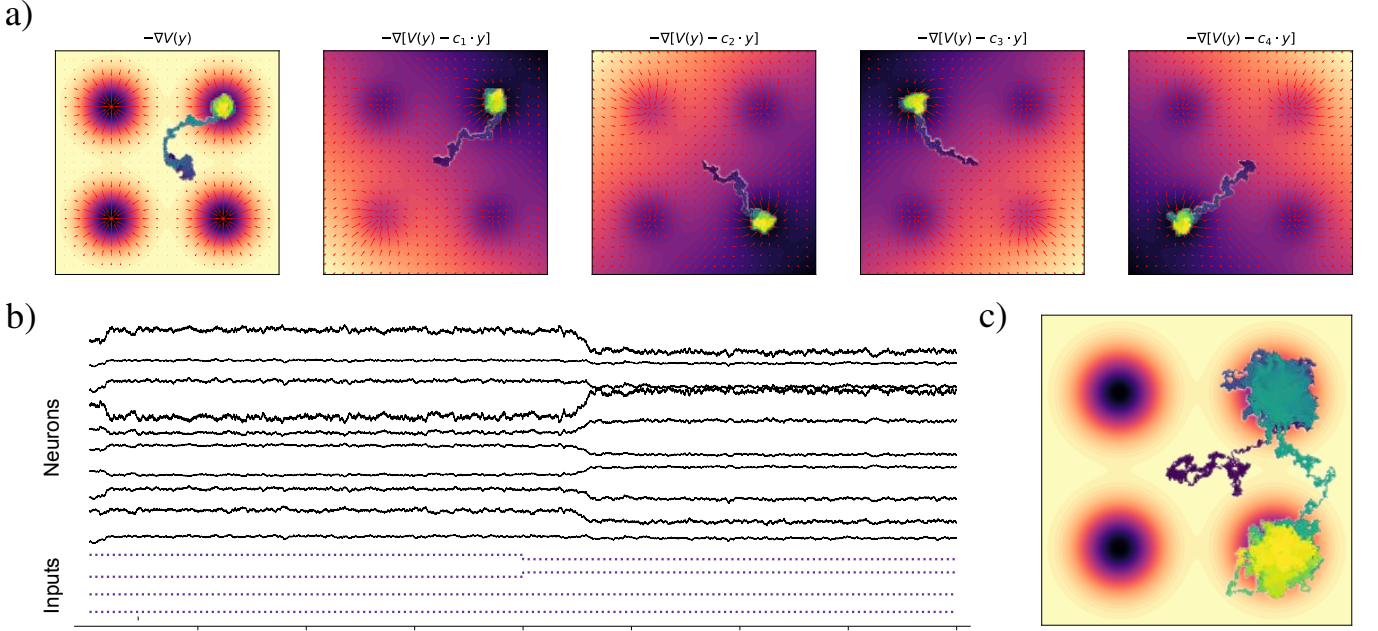


**FIG. 6. Input-driven attractor-switching.** *a)* We consider a four-well energy potential in the plane. In the absence of inputs, the trajectories converge to a minima at random, with a preference for the closest one. We can then tilt the potential with an input, which prioritises the relevant minima, and causes the trajectories to tend towards it. *b)* We train a 256-neuron RNN to embed the potential-gradient dynamics. Using a one-hot coding for the input, we learn the coupling matrix input connectivity and bias, then add the input to the RNN during integration. We start with the input that drives the process to the top-right well, then switch it halfway through to the bottom-right well. We plot traces from 10 random neurons and see the network dynamics react to the input and converge to the other minima. *c)* Projecting the RNN trajectory onto the latent space, we see the attractor-switching that occurs due to the change in input.

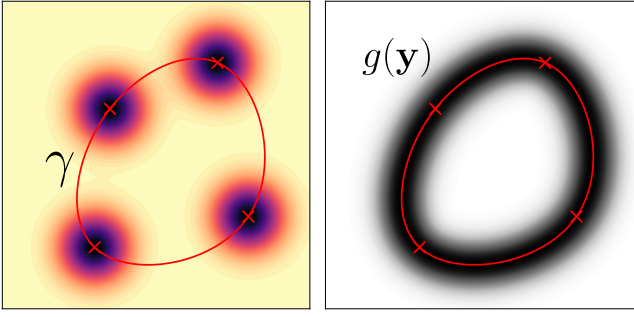


**FIG. 7. Constructing rotational diffusions.** To construct an SDE with rotation between energy minima, we begin with the gradient of the energy potential. We then draw a closed curve,  $\gamma$ , through the minima in the direction of rotation. From this, we can define a rotational drift which decays with distance from the curve due to the weighting kernel  $g(\mathbf{y})$ .

to rotate (Fig. 7). Next, we design a rotational field that provides a force in the direction of this closed curve, acting along all concentric curves with the same shape. For example, if the curve is a circle, this is the set of circles with the same centre but different radii. To do this, we consider  $\gamma = \partial O$ , to be the boundary of a bounded planar region  $O \subset P$ , and define the

signed distance to be,

$$\phi(\mathbf{y}) = \begin{cases} -\text{dist}(\mathbf{y}, \gamma) & \text{if } \mathbf{x} \in O \\ \text{dist}(\mathbf{y}, \gamma) & \text{if } \mathbf{x} \in P \setminus O \end{cases} \quad (37)$$

where  $\text{dist}(\mathbf{y}, \gamma) = \inf_{\mathbf{p} \in \partial O} \|\mathbf{y} - \mathbf{p}\|$ . This defines a potential where each level set is a closed curve with the same shape, up to an inflation or deflation, as  $\gamma$ . We would like our rotational field to be tangent to these level sets. We obtain such a field by rotating  $\nabla \phi$  by  $\pi/2$  via an antisymmetric matrix  $\mathbf{M}$ , which in  $\mathbb{R}^2$  is given by,

$$\mathbf{M} = \begin{pmatrix} 0 & 1 \\ -1 & 0 \end{pmatrix}. \quad (38)$$

To prevent the rotational field from dominating the gradient dynamics far from the minima, we also introduce a weighting kernel,

$$g(\mathbf{y}) = \exp\left(-\frac{\phi^2(\mathbf{y}, \gamma)}{2\xi^2}\right), \quad (39)$$

which decays exponentially with the distance from the closed curve  $\gamma$  at a rate inversely proportional to  $\xi^2$  (Fig. 7). Putting together the components, we have the rotational vector field,

$$\mathbf{R}(\mathbf{y}) = \frac{\alpha}{\pi(\mathbf{y})} g(\mathbf{y}) \mathbf{M} \nabla \phi(\mathbf{y}), \quad (40)$$

where  $\alpha$  is the scalar strength of rotation, and where  $\mathbf{R}$  is DFSD (see App. C). This gives a combined field,

$$\mathbf{f} = -\nabla V + \mathbf{R}, \quad (41)$$

that has both attractive and cycling dynamics. Given a set of points  $\{\mathbf{\mu}_j\}$  to encode as minima of a Gaussian potential, the parameters  $\{\{a_j\}, \{v_j\}, \sigma, \xi, \alpha\}$ , can all be chosen to obtain the desired behaviour in the process (details on parameters are given in App. H).

We construct three examples of diffusion processes with three, four, and five Gaussian wells placed in the plane. In the case of the three minima we choose the curve  $\gamma$  to be the intersecting circle, whilst for four and five minima we compute it numerically with cubic splines (see App. A 3). Fig. 8 illustrates the example processes for *a*) three, *b*) four, and *c*) five minima. Next, we use DDM to train a different 128-neuron RNN to approximate each diffusion process in a latent affine subspace. Once the model is trained, we sample trajectories from the RNN and project them into the learnt subspace. Fig. 9 shows example traces from ten randomly selected neurons in each network, as well as a projection of the trajectory and the drift into the affine subspace. We see that the RNN is able to encode such autonomous attractor-cycling dynamics in a neural subspace. Moreover, as in the case of the nonlinear systems (Fig. 2), the activity of individual neurons hints at the character of the encoded process i.e. here we see neuronal activity jumping between piecewise approximately constant segments.

#### IV. NONEQUILIBRIUM STEADY-STATES OF NEURAL NETWORKS

Computing properties of the NESS for a high-dimensional network is particularly challenging, except in the case of simple, solvable processes [53], as the FP equation is high-dimensional and its numerical solution is computationally intractable. However, in the case of a high-dimensional RNN encoding a low-dimensional stationary diffusion in an invariant subspace, the situation simplifies significantly.

We consider, as before, an RNN with state  $\mathbf{u}(t) \in \mathcal{A}$ , where the latent dynamics follow the SDE,

$$d\mathbf{y}(t) = \mathbf{f}(\mathbf{y}) dt + \sigma d\mathbf{w}(t), \quad (42)$$

which has a stationary density  $\pi_{\mathbf{y}}(\mathbf{y})$ . The stationary density of  $\mathbf{u}$  is given by the *pushforward measure* [57],<sup>4</sup>

$$\pi_{\mathbf{u}}(\mathbf{u}) = \frac{\pi_{\mathbf{y}}(\Gamma^{\dagger}(\mathbf{u} - \mathbf{b}))}{\sqrt{\det(\Gamma^{\dagger}\Gamma)}}. \quad (43)$$

With the stationary density, the HHD, stationary flux, and EPR can be computed, and is closely related between the latent and

network-level. Assuming that the HHD of the latent process is given by  $\mathbf{f} = \mathbf{f}_{\text{rev}} + \mathbf{f}_{\text{irr}}$ , we can decompose the network drift,  $\mathbf{F}$  as,

$$\begin{aligned} \mathbf{F} &= \mathbf{F}_{\text{rev}} + \mathbf{F}_{\text{irr}}, \\ \mathbf{F}_{\text{irr}}(\mathbf{u}) &= \Gamma \mathbf{f}_{\text{irr}}(\Gamma^{\dagger}(\mathbf{u} - \mathbf{b})), \\ \mathbf{F}_{\text{rev}}(\mathbf{u}) &= \Gamma \mathbf{f}_{\text{rev}}(\Gamma^{\dagger}(\mathbf{u} - \mathbf{b})), \end{aligned} \quad (44)$$

which additionally implies that the fluxes and EPRs also converge (see App. E).

We return to the example process with three minima given in Sec. III B. As the process has a solvable NESS, we can compute the HHD,  $\mathbf{f}_{\text{rev}} = -\nabla V$  and  $\mathbf{f}_{\text{irr}} = \mathbf{R}$ , as shown in Panel *a*) of Fig. 10. The reversible component balances the diffusion to maintain the process at stationarity, as seen in the example trajectory, whilst the irreversible component cycles around the curve  $\gamma$ . We then train a 64-neuron RNN to approximate the process in a latent affine subspace. Using the HHD of the example and Eq. (44), we define a decomposition of the high-dimensional dynamics in the ambient space, and sample trajectories from each component. Panel *b*) shows a trajectory from each of these components. As with the dynamics at the latent level, we see that the reversible dynamics keep the process near the minima, balancing the noise, whilst the irreversible dynamics show limit-cycle behaviour.

#### A. A Helmholtz-Hodge decomposition of the network

Whilst Eq. (44) is a decomposition of the high-dimensional dynamics, it is challenging to interpret, as each component is a high-dimensional vector field that we cannot visualise. Moreover, the decomposition is not related directly to the learnt network connectivity or input currents, only to the learnt affine subspace.

Instead, we now relate these components to a decomposition of the network itself. We assume that the HHD of the network can be written as,

$$\begin{aligned} \mathbf{F}_{\text{irr}}(\mathbf{u}) &= -\rho \mathbf{u} + W_{\text{irr}} h(\Gamma \mathbf{y} + \mathbf{b}) + I_{\text{irr}}, \\ \mathbf{F}_{\text{rev}}(\mathbf{u}) &= -(1 - \rho) \mathbf{u} + W_{\text{rev}} h(\Gamma \mathbf{y} + \mathbf{b}) + I_{\text{rev}}, \end{aligned} \quad (45)$$

where  $W = W_{\text{rev}} + W_{\text{irr}}$ ,  $I = I_{\text{rev}} + I_{\text{irr}}$ , and  $\rho \in [0, 1]$ . We also assume that these components respect the parameterisation,

$$\begin{aligned} W_{\text{rev}} &= \Gamma W_{s,\text{rev}}, & W_{\text{irr}} &= \Gamma W_{s,\text{irr}}, \\ I_{\text{rev}} &= \Gamma I_{s,\text{rev}} + (1 - \rho) \mathbf{b}, & I_{\text{irr}} &= \Gamma I_{s,\text{irr}} + \rho \mathbf{b}, \end{aligned} \quad (46)$$

which ensures that they are tangent to the affine subspace, and thus neither component causes the process to drift away from it. This also implies that we have a network decomposition that corresponds to the reversible and irreversible components of the dynamics. We can solve for these components, by writing the projected dynamics in the affine subspace,

$$\begin{aligned} \hat{\mathbf{f}}_{\text{irr}}(\mathbf{y}) &= -\rho \mathbf{y} + W_{s,\text{irr}} h(\Gamma \mathbf{y} + \mathbf{b}) + I_{s,\text{irr}}, \\ \hat{\mathbf{f}}_{\text{rev}}(\mathbf{y}) &= -(1 - \rho) \mathbf{y} + W_{s,\text{rev}} h(\Gamma \mathbf{y} + \mathbf{b}) + I_{s,\text{rev}}, \end{aligned} \quad (47)$$

<sup>4</sup>From this point on, we are implicitly constraining  $\mathbf{u} \in \mathcal{A}$  to avoid Dirac deltas in the expression.

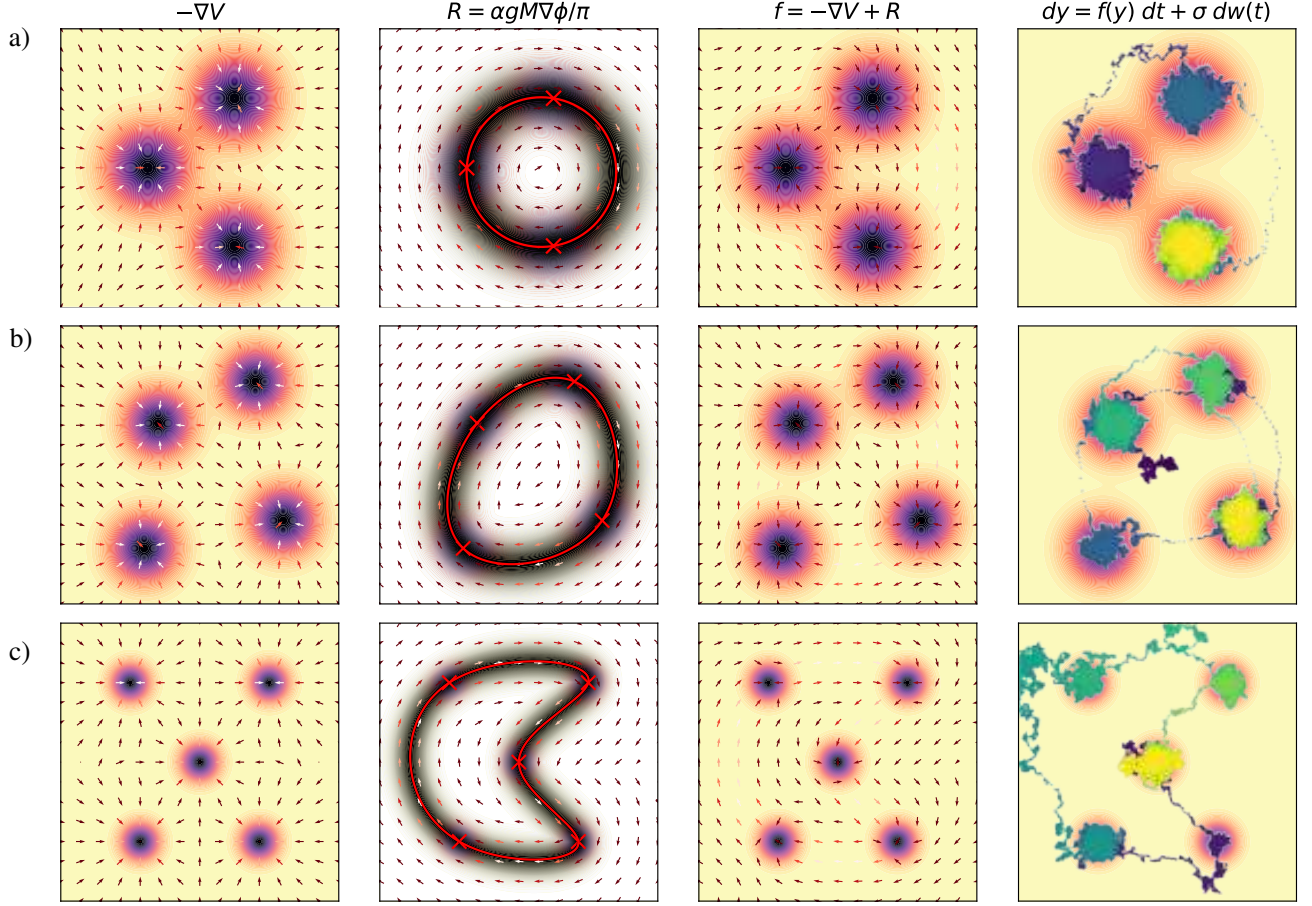


**FIG. 8. Attractor-cycling diffusions.** We construct example diffusion processes that cycle 3, 4, and 5 attractors with irreversible currents (Panels *a* – *c*). These are composed of a gradient flow (first column) plus a rotational component. The rotational component is constructed by taking a smooth curve through the minima, defining a potential as the distance from the curl, multiplying by a decaying weight kernel (contour in second column), and dividing by the stationary density (second column). Combined, this defines a vector field that both converges to, and cycles between attractors (third and fourth column).

where we can again notice that this can be seen as two two-layer perceptrons optimised to approximate a vector field, except that the weights and biases of the first layer are shared and already fixed,  $(\Gamma, \mathbf{b})$ , as is the sum of the weights and biases in the second layer i.e.  $W_s = W_{s,\text{rev}} + W_{s,\text{irr}}$  and  $I_s = I_{s,\text{rev}} + I_{s,\text{irr}}$ . We also introduce the trainable parameter  $\rho \in [0, 1]$ .

Whilst fixing the first layer causes this perceptron to no longer be a universal approximator, we find that this parameterisation is able to approximate the components with very high accuracy. This is due to the fact that  $(\Gamma, \mathbf{b})$  is optimised for the full drift field and therefore remains well-aligned with this downstream fine-tuning. This procedure yield a reversible-irreversible decomposition of the network structure that we can compare to the symmetric-asymmetric decomposition from Sec. II C.

Using the three minima example, we decompose the RNN with both the HHD and the symmetric-asymmetric decomposition. Panel *a*) of Fig. 11 shows the learnt HHD components of the vector field using Eq. (45), whilst Panels *b*) and *c*) show the decomposed connectivity matrix and bias vector, respectively. We find that for both decompositions, the

irreversible/asymmetric component has significantly larger weights, in absolute value, hinting that irreversible cycling dynamics require far higher network complexity.

In the appendix, we further investigate how the character of the target dynamics is represented in the RNN structure. In App. F, we show that the asymmetry of the RNN does not seem to be directly correlated with the EPR of the underlying process, a result that is in contrast with previous results for solvable networked systems [53]. In App. G, we describe how the DDM framework can be used to provide a universal representation for nonlinear systems and, using chaotic attractors as an example, we show how this can be used to compare their complexity.

## V. CONCLUSION

Neural circuits encode information and perform computations through a repertoire of complex spatiotemporal dynamics, but their fundamental mechanisms remain obscure. However, neural data analysis has shown that high-dimensional

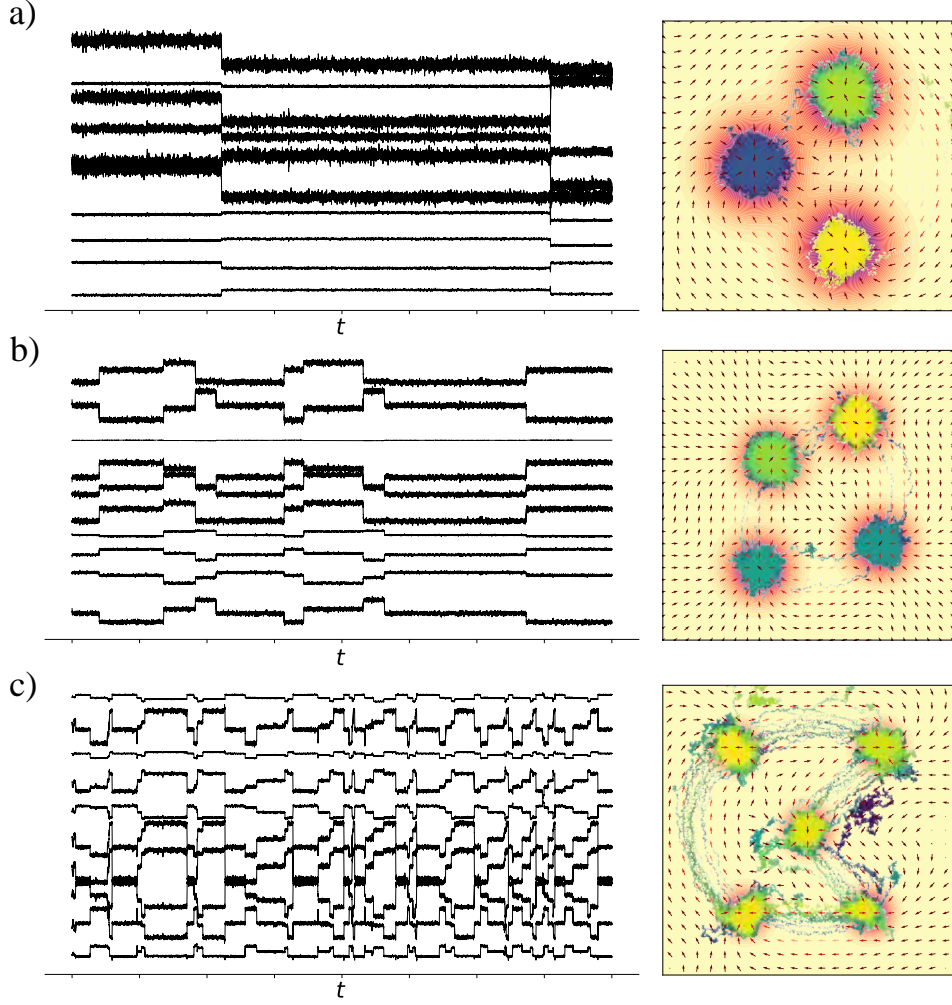


**FIG. 9. Attractor-cycling in RNNs.** We train 128-neuron RNNs to approximate the planar diffusion processes from Fig. 8 for *a)* three, *b)* four, and *c)* five minima respectively. Trajectories from the RNN can then be sampled autonomously, and the learnt drift can be projected onto the learnt affine subspace. We find that the RNNs are able to learn the target diffusion processes. For each RNN, we plot traces from ten random neurons. We see that the attractor cycling dynamics in the latent subspace are visible in the raw trajectories.

brain network dynamics are often redundant, with interpretable computational mechanisms best observed at the level of a latent neural manifold [25, 26, 33]. In line with previous studies focusing on the implications of low-rank structure in RNNs [27–29], our DDM framework presents a simple procedure to train a low-rank RNN to encode a arbitrary target SDE in an affine latent subspace, provided asymmetric connectivity is permitted. This allows us to go far beyond Hopfield’s original model [11], which was only able to encode attracting states as the minima of an energy-landscape, to encode nonlinear and nonequilibrium processes, such as chaotic attractors, and show that RNNs are able to perform both input-driven switching and autonomous cycling between attracting states. Finally, in an effort to elucidate the representation of the dynamics that is learnt by the RNN, we present two decompositions of the learnt connectivity matrix, using its asymmetry and its time-irreversibility respectively.

Whilst interesting, our approach brings with it a number of limitations. First, unlike Hopfield’s model which employs a

Hebbian learning rule, the DDM framework trains the RNN via backpropagation of error, noticing that a low-rank RNN is equivalent to a two-layer perceptron. This makes training quick, easy, and stable, unlike BPTT for RNNs, but is not biologically motivated or plausible. In this model, neural manifolds do not *emerge* spontaneously due to self-organisation, perhaps as the result of a learning rule. Instead, they are created by enforced structure in the connectivity. Most approaches enforce manifold structure through low-rank connectivity [28, 58], or by assuming certain symmetry properties [59, 60], but there have been some attempts to develop biologically-inspired learning rules for RNNs and other neural network models [5, 55, 61]. Nevertheless, the mechanisms by which biological neural circuits *learn* to encode complex dynamics over neural manifolds remain unclear, and requires the development of learning rules which produce asymmetric connectivity and emergent manifold structure. Next, our framework encodes dynamics in an affine linear subspace, suggesting that the relationship between neuronal states and

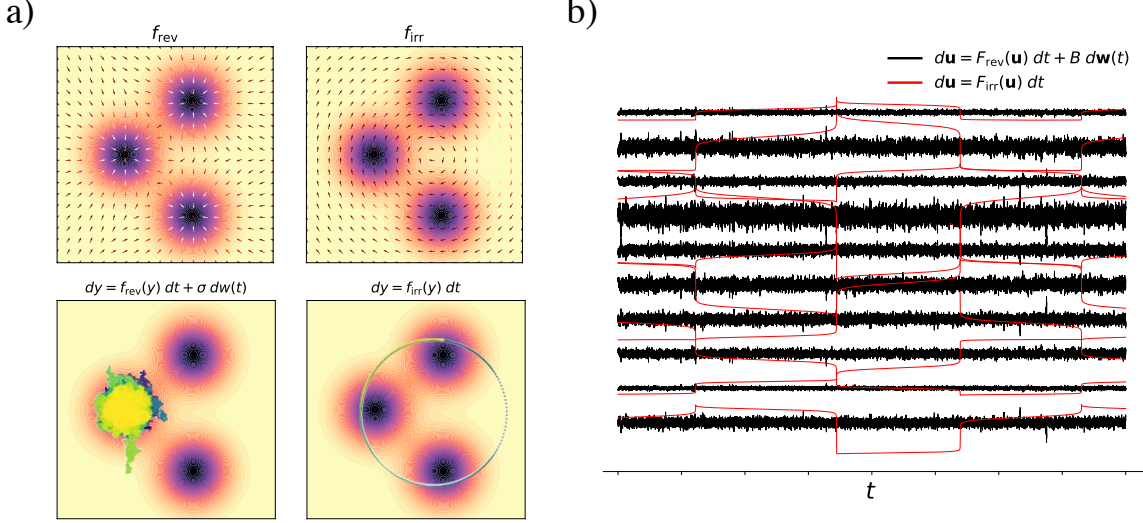


FIG. 10. **The HHD of a latent, embedded process.** a) When we embed a process with a known NESS, we can perform the HHD. In this example with three minima, we see that the reversible dynamics balance the diffusion and maintain the process on the stationary distribution, whilst the rotational dynamics create rotation around the curve  $\gamma$ . b) We train an RNN with 64 neurons to approximate the process in a latent affine subspace. Using the HHD and Eq. (44), we can define the irreversible,  $\mathbf{F}_{\text{irr}}$  and reversible,  $\mathbf{F}_{\text{rev}}$  components of the high-dimensional dynamics. We see that the reversible dynamics in the ambient space keep the process near the minima, balancing the noise, whilst the irreversible dynamics show limit-cycle behaviour in the ambient space.

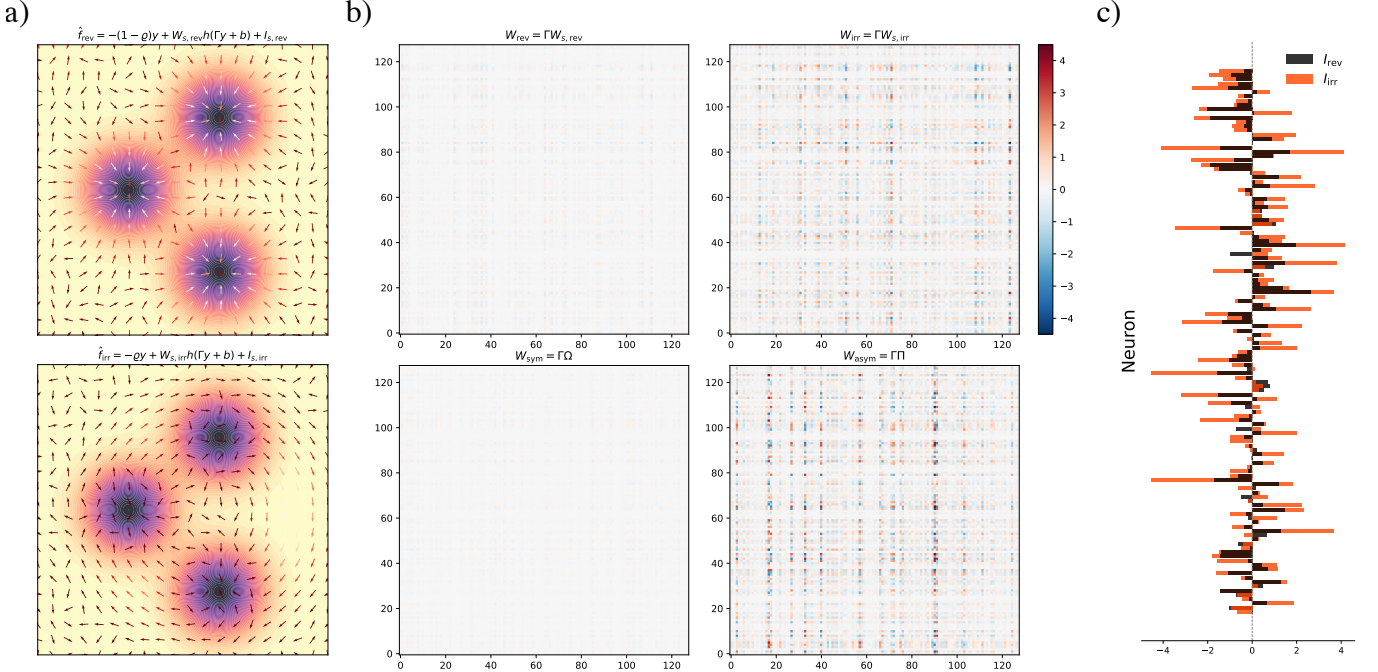


FIG. 11. **The HHD of an RNN.** a) Following Eq. (47), we train two coupled RNNs to approximate the reversible and irreversible components of the HHD respectively. Their projected drift shows that they were able to learn the components effectively. b) We can decompose the learnt connectivity matrix,  $W$ , using both the HHD,  $W = W_{\text{rev}} + W_{\text{irr}}$ , or using the symmetric-asymmetric decomposition from Sec. II C,  $W = W_{\text{sym}} + W_{\text{asym}}$ . We find that for this three minima example, the magnitude of the irreversible and asymmetric components are far greater than the reversible component suggesting that encoding rotational or cycling dynamics requires more network complexity. c) We can also examine the decomposition of the input current vector,  $I = I_{\text{irr}} + I_{\text{rev}}$ . As with the connectivity, more of the input current is used to encode the irreversible component than the reversible component.

neural manifolds is linear. Whilst linear methods have been used extensively to probe neural data [48], state-of-the-art approaches reveal neural manifolds with nonlinear dimensionality reduction [3, 25]. A more general relationship between neural firing and the effective computational manifold, allows for a much richer latent geometry in the system, which would be more consistent with empirical data. However, this produces major mathematical challenges to our framework, as nonlinear maps introduce troublesome Jacobian and Hessian terms in the projected dynamics. Finally, whilst we considered one case of a input-driven circuit, we mostly focus on autonomous RNN dynamics, which encode stationary processes. Integrating an RNN as the computational circuit in a more complete and time-dependent network, which includes both sensory input and an upstream output, is crucial for relating this model to more neuroscientific applications, such as motor control.

Asymmetric connections are required for RNNs to encode complex, nonlinear dynamics, and are intimately related to the emerging topic of nonequilibrium brain dynamics. At a range of scales, the brain has been shown to violate the detailed balance condition and produce time-irreversible dynamics [19]. Whilst nonequilibrium brain network dynamics have been linked to asymmetric connections between neurons and brain regions [18, 53, 62, 63], here we go beyond observational analysis of neural data, and present a possible computational *mechanism* for such nonequilibrium dynamics, indicating that time-irreversibility is the necessary result of computation in neural circuits. However, as discussed in App. F, we found that the asymmetry of the RNN was not directly correlated with the irreversibility of the encoded process. Related results have shown that irreversibility of neural dynamics is also uncorrelated with the irreversibility of sensory stimuli [64], thus the exact relationship between the nonequilibrium nature of sensory information, computational mechanisms, and observed dynamics remains unclear.

In an effort to understand how dynamics are represented by an RNN, it is interesting to study the properties of the inferred connectivity. In particular, as any symmetric component of the connectivity can be seen as encoding an energy landscape, probing the connectivity with matrix decompositions is a promising way forward. Furthermore, a number of decompositions for stochastic processes have been developed [42, 43, 65], which have implications for their nonequilibrium thermodynamics and their convergence to stationarity. We present avenues for exploring the relationship between components of the connectivity, and the components of the underlying target process.

The DDM framework provides a simple approach for encoding low-dimensional computational dynamics in a high-dimensional neural network. As a result, it marries the models of attractor neural networks with the theory of neural manifolds, providing us a way to investigate how cognitive processes may be represented by neural circuits. Ultimately, it brings us a step closer to cracking the neural code.

## CODE AVAILABILITY

Code will be made available upon publication at <https://github.com/rnartallo/ddm>.

## AUTHOR CONTRIBUTIONS

R.N.K. designed and performed research and wrote the manuscript. R.L. and A.G. designed and supervised the research and edited the manuscript.

## ACKNOWLEDGEMENTS

R.N.K would like to thank Pauline Thibaut for her pixel renditions of a dog and chick in App. D. Additionally, the authors would like to thank photographer Alexas Fotos for uploading their image of the labyrinth game for free use (Fig. 5).

R.N.K acknowledge support in the form of an EPSRC Doctoral Scholarship from Grants No. EP/T517811/1 and No. EP/R513295/1. R.L. acknowledges support from the EPSRC grants EP/V013068/1, EP/V03474X/1 and EP/Y028872/1

## SUPPLEMENTARY MATERIAL

### Appendix A: Numerical methods

#### 1. Simulating trajectories from SDEs

We sample paths from an SDE using the *Euler-Maruyama* discretisation,

$$\mathbf{x}_{t+\Delta t} = \mathbf{x}_t + \Delta t [\mathbf{f}(\mathbf{x}_t)] + \Delta \mathbf{w}_t [\Sigma(\mathbf{x}_t)], \quad (A1)$$

where  $\Delta t$  is the time-step and  $\Delta \mathbf{w}_t$  are independent and identically distributed (i.i.d.) multivariate normal random variables with mean zero and covariance  $\Delta t \mathbf{I}_n$  [66].

#### 2. Computing inputs for attractor-switching

In Sec. III A, we propose an approach for designing an RNN that switches between attractors based on an input. Here we present the concrete approach used for computing  $\mathbf{c}$ ,  $G_s$ , and  $\mathbf{d}$ , in the numerical example. As detailed in Sec. III A,  $\mathbf{c} \in \mathbb{R}^k$  makes the local minimum  $\boldsymbol{\mu}_{i^*}$  a global minimum if,

$$\mathbf{c} \cdot (\boldsymbol{\mu}_{i^*} - \boldsymbol{\mu}_j) > V_{i^*}^0 - V_j^0, \quad (A2)$$

for all  $j \neq i^*$ . Whilst this defines a convex subset, we will focus on finding a single value  $\mathbf{c}_i^*$  for each  $i$  by solving the quadratic convex problem,

$$\mathbf{c}_i^* = \operatorname{argmin}_{\mathbf{c} \in \mathbb{R}^k} \frac{1}{2} \|\mathbf{c}\|_2^2, \quad (A3)$$

$$\text{s. t. } \mathbf{c} \cdot (\boldsymbol{\mu}_i - \boldsymbol{\mu}_j) \geq V_i^0 - V_j^0 + \delta, \text{ for } j \neq i, \quad (A4)$$

where  $\delta > 0$  is a small parameter used to weaken the strict inequality. We solve this with convex optimisation in `cvxpy`. Given a collection of  $\{\mathbf{c}_j^*\}$ , we choose a coding for the inputs. For example, we can choose a ‘one-hot’ encoding where  $l = m$  i.e. we have one input direction per minimum, and  $\mathbf{s} = \mathbf{e}_i$  is the input corresponding to minimum  $i$ , where  $\mathbf{e}_i$  is the unit vector in the direction  $i$ . Alternatively, we can sample random Gaussian vectors for  $\mathbf{s}$ . In any case, we can also add low-intensity noise to the input. It remains to solve for  $G_s$  and  $\mathbf{d}$  given the coding scheme, for which we use *ridge regression* [67]. We combine our  $\mathbf{c}^*$  values into a matrix  $\mathbf{C} \in \mathbb{R}^{m \times k}$ , and combine the codes  $\mathbf{s}_i$  into a matrix  $\mathbf{S} \in \mathbb{R}^{m \times m}$ , and augment it with an additional column of ones to form  $\mathbf{S}^* = [\mathbf{S}, \mathbf{1}] \in \mathbb{R}^{m \times (m+1)}$ . We then aim to fit the model  $\mathbf{C} \approx \mathbf{S}\mathbf{G}_s + \mathbf{1}\mathbf{d}^\top$ , by minimising,

$$\Theta^* = \operatorname{argmin}_{\Theta} \|\mathbf{S}^*\Theta - \mathbf{C}\|^2 + \lambda \|\Theta\|^2, \quad (\text{A5})$$

where  $\Theta = [G_s, \mathbf{d}]$ . This has exact solution,

$$\Theta^* = ((\mathbf{S}^*)^\top \mathbf{S}^* + \lambda \mathbf{I})^{-1} (\mathbf{S}^*)^\top \mathbf{C}. \quad (\text{A6})$$

### 3. Constructing closed curves with splines

We compute interpolating closed curves with cubic splines with periodic boundary conditions. More specifically we use `CubicSpline` from `scipy.interpolate` [68]. We then parametrise the curve,  $\gamma(t)$ , with 500 time-points and construct a `matplotlib` path. We can then measure the distance between any point,  $p$ , and each discrete point in the path, taking the minimum to be the distance between  $p$  and  $\gamma$ .

## Appendix B: Optimal decomposition of a network under constraints

Let  $W \in \mathbb{R}^{n \times n}$  be a matrix that is low-rank and has the form  $W = \Gamma W_s$ , where  $\Gamma \in \mathbb{R}^{n \times k}$  and  $W_s \in \mathbb{R}^{k \times n}$ .  $\Gamma$  has full column rank  $k$ . We want to find the ‘best’ decomposition,

$$W = \Gamma(\Omega + \Pi), \quad (\text{B1})$$

where  $\Gamma\Omega$  is symmetric. We will define this optimal decomposition to have,

$$\tilde{\Omega} = \operatorname{argmin}_{\Omega} \|\Gamma\Omega - C\|_F^2, \quad (\text{B2})$$

where  $C = \frac{1}{2}(W + W^\top)$  i.e. the matrix that is most similar to the symmetrised version of  $W$ , but which respects the parametrisation.

Let  $P$  be the projector matrix onto

$$\mathcal{S} = \{X \in \mathbb{R}^{n \times n} : X \in \operatorname{range}(\Gamma)\}, \quad (\text{B3})$$

i.e.  $P = \Gamma\Gamma^\dagger$ . Due to the symmetry of any feasible  $X$ , we have that both the columns and rows of  $X$  live in the range of  $\Gamma$ . This implies that,

$$PX = X, \quad XP = X, \quad (\text{B4})$$

which implies that  $X = PXP$  for any feasible  $X$ .

As we are trying to minimise the Frobenius norm, the optimal solution  $X = \Gamma\Omega$ , is the projection of  $C$  onto the linear subspace,

$$\mathcal{Q} = \{X \in \mathbb{R}^{n \times n} : X = X^\top, X \in \operatorname{range}(\Gamma)\}. \quad (\text{B5})$$

As  $C$  is already symmetric, the solution is simply the projection of  $C$  onto  $\mathcal{S}$ ,

$$X = PCP = \Gamma\Gamma^\dagger C\Gamma\Gamma^\dagger, \quad (\text{B6})$$

which gives,

$$\tilde{\Omega} = \Gamma^\dagger C\Gamma\Gamma^\dagger. \quad (\text{B7})$$

## Appendix C: Designed rotational drift is DFSD

In the example considered in Sec. III, we consider a rotational field of the form,

$$\mathbf{R}(\mathbf{y}) = \frac{\alpha}{\pi(\mathbf{y})} g(\mathbf{y}) \mathbf{M} \nabla \phi(\mathbf{y}). \quad (\text{C1})$$

We can show that this field is DFSD by showing that,

$$\boldsymbol{\zeta}(\mathbf{y}) = g(\mathbf{y}) \mathbf{M} \nabla \phi(\mathbf{y}), \quad (\text{C2})$$

is divergence-free. Applying the product rule we have that,

$$\nabla \cdot \boldsymbol{\zeta} = (\nabla g) \cdot (\mathbf{M} \nabla \phi) + g(\nabla \cdot (\mathbf{M} \nabla \phi)). \quad (\text{C3})$$

We have that,

$$\nabla g = -\frac{\phi}{\xi^2} g \nabla \phi, \quad (\text{C4})$$

which implies that,

$$\begin{aligned} (\nabla g) \cdot (\mathbf{M} \nabla \phi) &= -\frac{\phi}{\xi^2} g \nabla \phi \cdot (\mathbf{M} \nabla \phi), \\ &= 0, \end{aligned} \quad (\text{C5})$$

as  $\mathbf{v} \cdot \mathbf{M}\mathbf{v} = 0$  for antisymmetric  $\mathbf{M}$ . Next, we have that,

$$\nabla \cdot (\mathbf{M} \nabla \phi) = \sum_{i,j} \mathbf{M}_{ij} \partial_i \partial_j \phi, \quad (\text{C6})$$

which is the sum-product of a symmetric (Hessian) and anti-symmetric matrix, which is zero. Thus  $\nabla \cdot \boldsymbol{\zeta} = 0$ .

## Appendix D: Attractor-cycling diffusions in higher-dimensions

In this section, we consider similar approaches to that of Sec. III for designing SDEs with transiently visited attractors. First, we consider a high-dimensional example that cycles between two pixelated images. Next, we consider a three-dimensional example where the attracting points are non-coplanar. Unlike the examples in Sec. III, we do not encode these processes in the dynamics of a RNN as it is not motivated to encode a high-dimensional process on a neural manifold, and the non-coplanar example is not smooth.

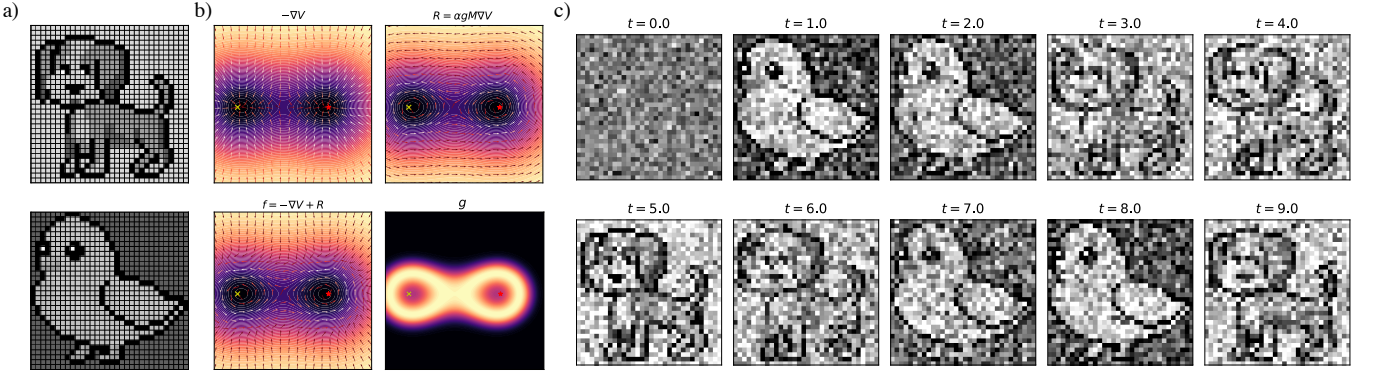


FIG. 12. **Cycling between pixelated images in high-dimensions.** We can modify our approach from Sec. III to design processes which cycle between energy minima in high-dimensions. *a)* We illustrate this using  $32 \times 32$  pixelated images of a dog and a chick, which are points in  $\mathbb{R}^{1024}$ . *b)* As before, we design a drift field that encodes these points as the minima of a Gaussian potential, but drives rotation between them without disrupting the stationary density. *c)* Integrating this SDE, we can sample paths which cycle between (noisy) instances of the two images in the high-dimensional space.

### 1. A high-dimensional example with pixel images

We consider two grey-scaled,  $32 \times 32$  images, whose pixel-values are scaled to  $[0, 1]$ . Panel *a*) of Fig. 12 shows a dog and chick image, respectively. These points can be thought of as points  $\mu_1, \mu_2 \in \mathbb{R}^{1024}$ . We define a Gaussian potential on  $\mathbb{R}^{1024}$  with minima at the points corresponding to the dog and chick images respectively. Next, we want to create a rotational flow that cycles between these pixelated images in  $\mathbb{R}^{1024}$ . To do this, we first select a plane which intersects both these points – we choose the one that goes through the origin – which is spanned by vectors  $\{\mathbf{e}_1, \mathbf{e}_2\}$ , using the Gram-Schmidt orthogonalisation. We take  $\mathbf{d} = \mu_2 - \mu_1$ , and  $\mathbf{e}_1 = \mathbf{d}/\|\mathbf{d}\|$ . Next, we must choose a vector which is linearly independent of  $\mathbf{e}_1$ , so we choose the standard basis vector in the direction where  $\mathbf{e}_1$  has smallest absolute value,  $\mathbf{e}_k$ , and then project this vector onto  $\mathbf{e}_1$ ,

$$\mathbf{q} = \mathbf{e}_k - (\mathbf{e}_k \cdot \mathbf{e}_1)\mathbf{e}_1, \quad (\text{D1})$$

and then normalise it to obtain  $\mathbf{e}_2 = \mathbf{q}/\|\mathbf{q}\|$ . The result is an orthonormal basis,  $\{\mathbf{e}_1, \mathbf{e}_2\}$ , for a 2D plane that intersects both minima.

Given this plane, the matrix representing a  $\pi/2$  rotation in the plane, is given by,

$$\mathbf{M} = \mathbf{e}_2 \otimes \mathbf{e}_1 - \mathbf{e}_1 \otimes \mathbf{e}_2, \quad (\text{D2})$$

where  $\otimes$  is the outer product. We define the rotational component to be,

$$\mathbf{R}(\mathbf{y}) = \alpha g(\mathbf{y}) \mathbf{M} \nabla V(\mathbf{y}), \quad (\text{D3})$$

where we are rotating the gradient field itself. Note that we have not defined an intersecting curve as in Sec. III. Instead, we modify the weighting kernel,

$$g(\mathbf{y}) = \exp\left(-\frac{(V(\mathbf{y}) - s)^2}{2\xi^2}\right), \quad (\text{D4})$$

such that it decays with the distance from a particular level set of the potential function with value  $s$ , rather than the distance from a curve. As a result, the rotational field creates flow along this particular level set, pushing trajectories between the minima. It is easy to show that this is DFSD. Finally, we define our combined drift field to be,

$$\mathbf{f} = -\nabla V + \mathbf{R}, \quad (\text{D5})$$

thus it admits a stationary Boltzmann distribution. The gradient flow, rotational component, weighting kernel, and combined field are projected onto the plane in Panel *b*) of Fig. 12. Integrating the SDE with this drift field, and suitably chosen noisy intensity, defines a process whose trajectories cycle between (noisy) instances of the two images in succession, as shown in Panel *c*) of Fig. 12.

### 2. Non-coplanar minima in three dimensions

Here we consider a set of minima which are non-coplanar in  $\mathbb{R}^3$ . As before, we define the attractor dynamics,  $-\nabla V$ , with Gaussian wells. However, the rotational component  $\mathbf{R}$  from the coplanar case cannot be applied in this setting. This is because the level sets of the signed distance function are no longer curves, but instead tubular sections. As a result, flows along the contours of these level sets are not restricted to the ‘direction’ of the curve through the minima, but also along the minor radius of each tube. Instead, we introduce an alternative approach.

Again, we draw a differentiable curve,  $\gamma$ , that intersects our minima in the order that we wish them to be traversed. Fig. 13 shows an example with four minima which lie on saddle. Panel *a*) shows the intersecting curve. Next, we consider the *tubular neighbourhood*,  $Q$ , around the non-coplanar curve with parameterisation  $\gamma(s)$ , which is defined as,

$$Q = \{\mathbf{y} \in \mathbb{R}^3 : \text{dist}(\mathbf{y}, \gamma) < r\}, \quad (\text{D6})$$

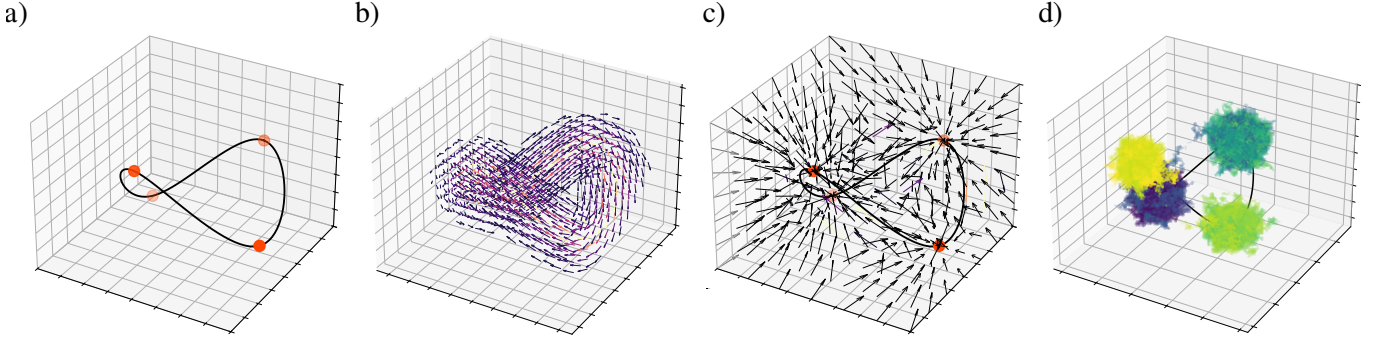


FIG. 13. **Cycling between non-coplanar minima.** We can also design SDEs which cycle between non-coplanar minima in 3D. *a*) In this example, we consider four minima on a saddle, which we interpolate with a cubic spline. *b*) We design a rotational field which pushes trajectories around this curve, but is DFSD. *c*) This produces a combined field which has both attracting and rotational dynamics. *d*) Sampling from this process, we see that it rotates transiently between attracting states.

where  $r$  is the *tubular radius*, which must be smaller than the *injectivity radius*  $r_{\max} = \kappa_{\max}^{-1}$ , where  $\kappa_{\max}$  is the maximum curvature of  $\gamma$  – this is the largest tube that does not self-intersect. Each point  $\mathbf{y} \in Q$  can be written as,

$$\mathbf{y}(s, \rho, \theta) = \gamma(s) + \rho \cos(\theta) \cdot \mathbf{N}(s) + \rho \sin(\theta) \cdot \mathbf{B}(s), \quad (\text{D7})$$

where  $s$  is the arc-length parameter, and  $(\rho, \theta)$  are polar coordinates in the *normal plane* spanned by the *normal* and *bi-normal* vectors,  $\{\mathbf{N}(s), \mathbf{B}(s)\}$  at  $\gamma(s)$  [69, 70]. At any point  $\gamma(s)$ , we can form a local cylindrical coordinate system,

$$\begin{aligned} \mathbf{e}_s &= \mathbf{T}(s) \\ \mathbf{e}_\rho &= \cos(\theta) \cdot \mathbf{N}(s) + \sin(\theta) \cdot \mathbf{B}(s) \\ \mathbf{e}_\theta &= -\sin(\theta) \cdot \mathbf{N}(s) + \cos(\theta) \cdot \mathbf{B}(s) \end{aligned} \quad (\text{D8})$$

which are the *axial*, *radial* and *azimuthal* basis vectors respectively, and  $\mathbf{T}(s)$  is the *tangent* vector to  $\gamma(s)$  [69]. Together, the vectors  $\{\mathbf{T}(s), \mathbf{N}(s), \mathbf{B}(s)\}$  form the *Frenet-Serret* orthonormal frame along a curve [69]. This cylindrical basis is accurate up to a first-order correction arising due to the curvature of the curve. Our goal is to construct a vector field with forcing in the direction  $\mathbf{T}(s)$ . To do so, we define the vector potential,

$$\mathbf{A}(s, \rho, \theta) = \psi(\rho) \mathbf{e}_\theta(s, \rho, \theta), \quad (\text{D9})$$

where  $\psi(\rho) = \exp(-\rho^2/2\xi^2)$  is the weighting kernel that decays as  $\rho$  increases i.e. that decays with distance from  $\gamma$ . This coincides with our definition of  $g$  in the planar case (Eq. (39)). We can take the curl to obtain a divergence-free field,  $\nabla \times \mathbf{A}(\mathbf{x})$ , which, following the right hand rule, pushes in the direction  $\mathbf{T}(s)$ . In practice, the curl of the vector potential is approximated numerically using finite differences. Finally, dividing through by the stationary density, we obtain,

$$\mathbf{R}(\mathbf{y}) = \frac{\alpha}{\pi(\mathbf{y})} \nabla \times \mathbf{A}(\mathbf{y}), \quad (\text{D10})$$

where  $\alpha$  controls the strength of rotation. This field is DFSD, thus  $-\nabla V + \mathbf{R}$  converges to the Boltzmann density, yet pushes trajectories along  $\gamma$ , as desired. Panels *b*) and *c*) of Fig. 13

show the rotational component and combined vector field respectively, whilst Panel *d*) shows an example trajectory from this process. It cycles autonomously between the attractors exhibiting metastability. As there is a discontinuity between the field inside the tubular radius and beyond it, the field is not smooth, thus we not attempt to encode it in an RNN.

#### Appendix E: Nonequilibrium steady-state is equivalent between latent and network dynamics

Analytical results for the NESS of large, complex networks, including RNNs, are typically intractable, except for limited cases. We consider the situation where the RNN encodes a latent process with a known NESS. As considered in Sec. IV, we take an RNN with state  $\mathbf{u}(t) \in \mathcal{A}$ , where the latent dynamics follow the SDE,

$$d\mathbf{y}(t) = \mathbf{f}(\mathbf{y}) dt + B_s d\mathbf{w}(t), \quad (\text{E1})$$

which has a stationary density  $\pi_{\mathbf{y}}(\mathbf{y})$ . In the network space, as the mapping between latent and network trajectories is one-to-one,  $\mathbf{u}$  is given by the pushforward measure [57],

$$\pi_{\mathbf{u}}(\mathbf{u}) = \frac{\pi_{\mathbf{y}}(\Gamma^{\dagger}(\mathbf{u} - \mathbf{b}))}{\sqrt{\det(\Gamma^{\dagger} \Gamma)}}, \quad (\text{E2})$$

where we are restricting to  $\mathbf{u} \in \mathcal{A}$  to avoid Dirac-delta terms. Similarly, the flux is related by,

$$\mathbf{J}_{\mathbf{u}}(\mathbf{u}) = \frac{\Gamma \mathbf{J}_{\mathbf{y}}(\Gamma^{\dagger}(\mathbf{u} - \mathbf{b}))}{\sqrt{\det(\Gamma^{\dagger} \Gamma)}}. \quad (\text{E3})$$

Finally, we can compute the EPR. As mentioned in Sec. IV, the traditional formula for EPR, Eq. (29), assumes that the diffusion matrix is full-rank [56]. This does not hold in our case where  $D = BB^{\top} = \Gamma B_s B_s^{\top} \Gamma^{\top}$ , which is a symmetric positive semidefinite matrix with rank  $k$ . However, we can extend the EPR formula to this case, where it is given by,

$$\Phi = \int_{\mathbb{R}^n} \mathbf{F}_{\text{irr}}^{\top} D^{\dagger} \mathbf{F}_{\text{irr}} \pi_{\mathbf{u}} d\mathbf{u}, \quad (\text{E4})$$

i.e. where  $D^{-1}$  has been replaced by the MP inverse, if and only if  $\mathbf{F}_{\text{irr}}(\mathbf{u}) \in \text{Range}(B(\mathbf{u}))$  where  $B = \Gamma B_s$  [42]. We consider spatially-constant diffusion, and as we have already shown that  $\mathbf{F}_{\text{irr}}$  lies in the image of  $\Gamma$  (Eq. (44)), it is sufficient for  $B_s$  to be of full row-rank  $k$ , guaranteeing that the noise is *elliptic*. A necessary requirement for this is that  $d \geq k$  i.e. we have more independent noise-sources in the network than dimensions in the latent process. When  $B_s$  has full row-rank, we have that the EPR of the latent process and the full network are identical,

$$\Phi_{\mathbf{u}} = \Phi_{\mathbf{y}}. \quad (\text{E5})$$

#### Appendix F: Network asymmetry and entropy production

Neural systems operate in NESSs across a range of scales, with the level of irreversibility, defined by the EPR in Eq. (29), being correlated with the level of consciousness or the complexity of a cognitive task [19]. Moreover, the EPR has been shown to be driven by the asymmetry of the network underlying the neural activity [53]. Here, we investigate this further by considering a nonequilibrium diffusion with a parametrisable EPR, embedding the process in a latent subspace of a fixed-size RNN, and measuring the asymmetry of the resulting connectivity.

In particular, we consider the stochastic *Hopf oscillator*, a nonlinear model with a solvable NESS, which is given by,

$$d \begin{pmatrix} y_1(t) \\ y_2(t) \end{pmatrix} = \begin{pmatrix} (1 - y_1^2 - y_2^2)y_1 - \omega y_2 \\ (1 - y_1^2 - y_2^2)y_2 + \omega y_1 \end{pmatrix} dt + \sigma \begin{pmatrix} w_1(t) \\ w_2(t) \end{pmatrix}, \quad (\text{F1})$$

where  $\omega$  is the frequency of oscillation [19]. The NESS is given by a radially-symmetric stationary density and, for fixed  $\sigma$ , has EPR  $\Phi \propto \omega^2$ , satisfying time-reversibility if and only if  $\omega = 0$  (see Ref. [71]).

To measure the asymmetry of the resulting RNN, we consider the canonical symmetric-antisymmetric decomposition, the low-rank symmetric-antisymmetric decomposition of Sec. II C, and the HHD of Sec. IV. In general, this produces a pair  $(W_1, W_2)$  where  $W = W_1 + W_2$ , where we quantify the relative energy of  $W_1$  with,

$$\mathcal{E}(W_1, W_2) = \frac{|W_1|}{|W_1| + |W_2|}, \quad (\text{F2})$$

where  $|\cdot|$  is the Frobenius norm. We train an ensemble of 100 RNNs to encode the stochastic Hopf oscillator for each value in a range  $\omega \in [0, 5]$ . Fig. 14 shows the relative energy of *a*)  $(W - C, C)$ , *b*)  $(\Gamma\Pi, \Gamma\Omega)$ , and *c*)  $(W_{\text{irr}}, W_{\text{rev}})$ . Panel *d*) shows the fitted value of  $\rho$  from the network HHD in Eq. (45). We find that there is no clear relationship between the relative energy in the asymmetric/irreversible component and the EPR, which suggests that irreversible currents are also parametrised in the bias terms, and that the projection matrix  $\Gamma$  can induce asymmetries that are not trivially related to the rotational forces in the target vector field. This result contrasts with previous studies suggesting that the EPR is driven directly by network asymmetry [53], although this was not in the case of a low-rank system.

#### Appendix G: Measuring the complexity of dynamics with a universal representation

Whilst existing approaches include the calculation of Lyapunov exponents, Kaplan-Yorke embedding dimension, or the entropy rate, there is no consensus on how to measure the ‘complexity’ of a chaotic system [44]. Even at a descriptive level it can be difficult to define what is a more or less complex dynamics. For example, if time is rescaled so that an attractor is traversed at twice the speed, or an attractor is inflated in space, is it of the same complexity?

Whilst this fundamental problem remains, our embedding approach provides a universal representation of a nonlinear system via an RNN. The connectivity structure of the RNN can then be studied to derive a metric for the complexity of the representation, which in turn captures some features of the complexity of the encoded chaotic system. To illustrate this, we consider four familiar 3D chaotic attractors: the Lorenz and Dadras attractors introduced in Sec. II D, the *Rössler* attractor,

$$d \begin{pmatrix} y_1(t) \\ y_2(t) \\ y_3(t) \end{pmatrix} = \begin{pmatrix} -y_2 - y_3 \\ y_1 + ay_2 \\ b + y_3(y_1 - c) \end{pmatrix} dt, \quad (\text{G1})$$

with  $a = b = 0.2$  and  $c = 5.7$ , and the *Halvorsen* attractor,

$$d \begin{pmatrix} y_1(t) \\ y_2(t) \\ y_3(t) \end{pmatrix} = \begin{pmatrix} -ay_1 - 4y_2 - 4y_3 - y_2^2 \\ -ay_2 - 4y_3 - 4y_1 - y_3^2 \\ -ay_3 - 4y_1 - 4y_2 - y_1^2 \end{pmatrix} dt, \quad (\text{G2})$$

with  $a = 1.7$  [44]. For each of these systems, we train 100 separate RNNs, with 1024 neurons each, to encode the deterministic drift i.e. we set  $\lambda_{\text{diff}} = 0$ . With the fitted connectivity matrix,  $W$ , we then compute the *spectral radius*,

$$r(W) = \max_i |\lambda_i|, \quad (\text{G3})$$

where  $\lambda_i$  are the eigenvalues of  $W$ , and the *participation ratio* (PR),

$$\text{PR}(\mathbf{v}) = \frac{(\sum_i \mathbf{v}_i)^2}{N \sum_i \mathbf{v}_i^2}, \quad (\text{G4})$$

for each eigenvector  $\mathbf{v}$ . We can take the mean of the PR over all eigenvectors, or focus on the PR of the dominant mode. The spectral radius captures the maximum asymptotic growth of the system, and the degree of instability for fixed points and periodic trajectories. On the other hand, the participation ratio captures the effective proportion of neurons in the network that are active in encoding a representation. A PR of  $1/N$  implies that a single neuron encodes a representation, whilst a PR of 1 implies the entire network is being used to encode a representation.

Fig. 15 shows the *a*) spectral radius, *b*) PR of the dominant mode, and *c*) mean PR, for each system and its RNN representations. Whilst there is a lack of ‘ground truth’ for this exploratory experiment, we can notice that the Lorenz system has, by far, the highest spectral radius, suggesting that it

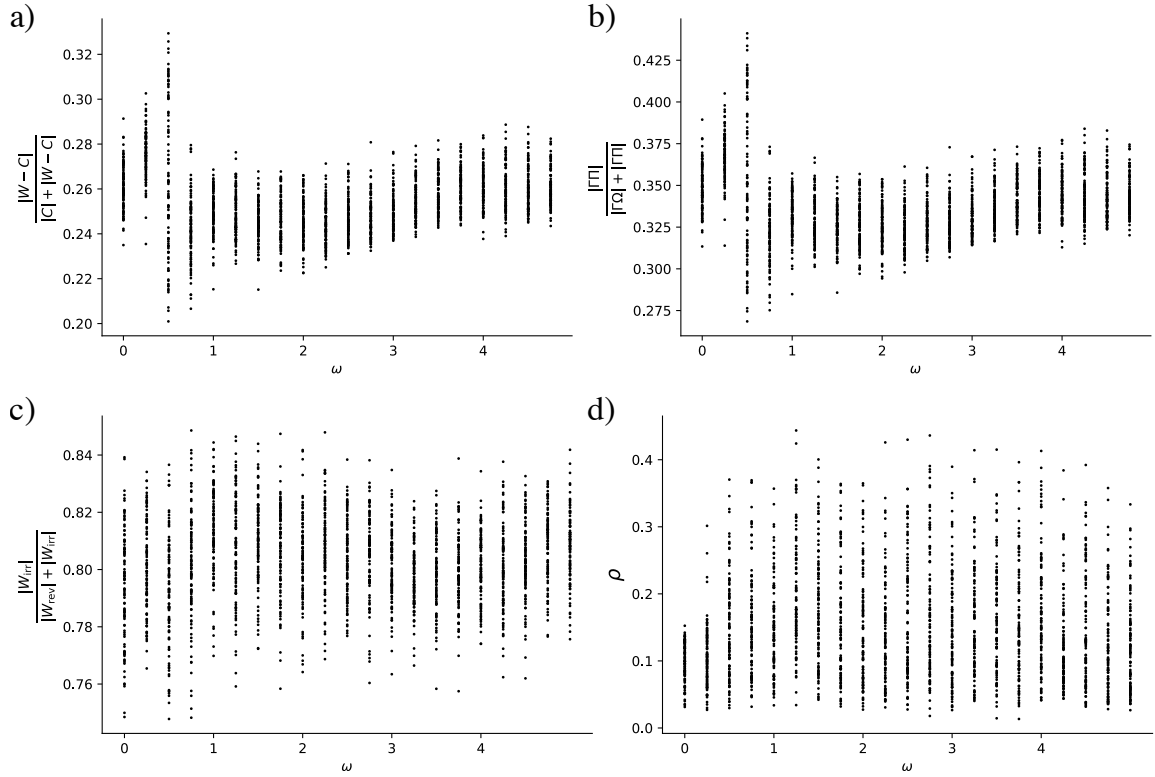


FIG. 14. **Network asymmetry for increasing EPR.** For a range of values  $\omega \in [0, 5]$  we train an ensemble of 100 RNNs. We then compute the relative size of each component in the decomposition with Eq. (F2) for *a*)  $(W - C, C)$ , *b*)  $(\Gamma\Pi, \Gamma\Omega)$ , and *c*)  $(W_{\text{irr}}, W_{\text{rev}})$ . In *d*) we also plot  $\rho$  from the network HHD in Eq. (45).

has the most instability and asymptotic growth. On the other hand, it is the Dadas attractor which has the highest mean PR and dominant PR, suggesting that it requires the most network complexity to be encoded. This is consistent with the fact that it has the most ‘scrolls’ and thus has non-trivial dynamics in the largest number of directions.

These results are just a first attempt at exploring the complexity of nonlinear systems via the unified and comparable representation offered by DDM, and further progress will require investigating additional network properties beyond those considered here in order to fully capture the richness of the underlying dynamics.

## Appendix H: Parameters and details for numerical experiments

Here we provide details on parameters for the numerical simulations. Throughout, we will train the perceptrons with PyTorch using the Adam optimiser with learning rate = 0.001. We fix  $\lambda_{\text{diff}} = 20$ .

### 1. Nonlinear systems and RNN representations

In Sec. II, we use the following parameters.

- **Van der Pol.** We take  $\sigma = 0.25$ . We train an RNN with

$N = 64$ , and 25,000 uniform samples from  $[-4, 4]^2$  for 30,000 epochs.

- **Lorenz.** We take  $\sigma = 0.25$ . We train an RNN with  $N = 512$ , and 125,000 uniform samples from  $[-25, 25] \times [-30, 30] \times [0, 50]$  with  $\lambda_{\text{diff}} = 20$  for 100,000 epochs.
- **Dadras.** We take  $\sigma = 0.01$ . We train an RNN with  $N = 1024$ , and 150,000 uniform samples from  $[-20, 20] \times [-12, 10] \times [-15, 15]$  for 100,000 epochs.

## 2. Switching and cycling attractors

In Sec. III, we use the following parameters.

- **Input-driven switching.** We place four minima at  $(\pm 3, \pm 3) \in \mathbb{R}^2$ , with Gaussian well parameters given by  $a_j = 0.125$  and  $v_j = 1$ , and noise intensity  $\sigma = 0.1$ . We train the RNN with  $N = 256$  using 25,000 samples from  $[-4, 4]^2$  for 30,000 epochs.

Next, we have the three examples of autonomously cycling diffusions.

- **Three minima.** We place three minima at  $\mu = \{(1, 2), (-1.5, 0), (1, -2.25)\}$ , with  $a_j = 0.25$  and  $v_j = 0.75$ . The process has  $\xi = 0.2$ ,  $\alpha = 1.5$  and  $\sigma = 0.2$ .

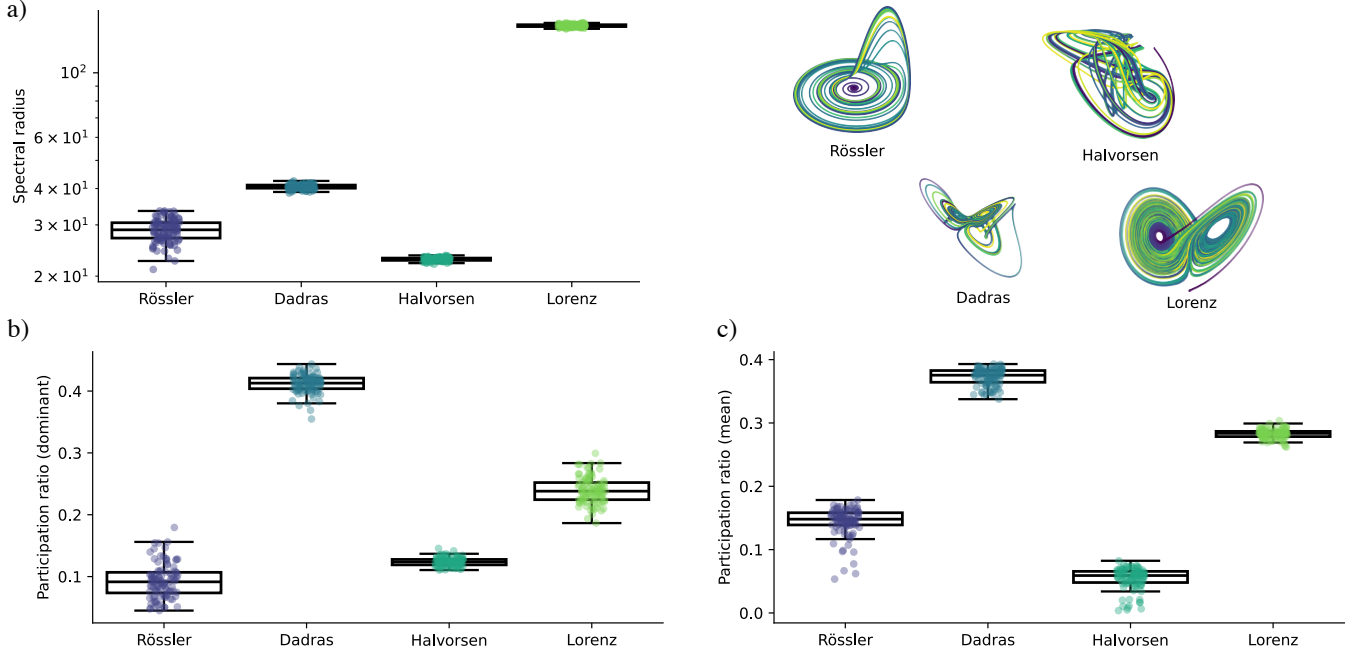


FIG. 15. **A universal representation for nonlinear dynamics.** The DDM framework allows us to obtain a universal representation for nonlinear dynamics. By studying the inferred parameters, we can define measures of ‘complexity’ for the dynamics and their representations. We illustrate this with chaotic attractors, where we compute the *a*) spectral radius, *b*) mean participation ratio, and *c*) participation ratio of the dominant mode, for the connectivity,  $W$ , of 100 RNNs with 1024 neurons each, trained to encode the Rössler, Dadras, Halvorsen, and Lorenz attractors. We find that the Lorenz attractor has, by far, the highest spectral radius, whilst the Dadras attractor has the highest participation ratio.

We train a RNN with  $N = 128$  and 25,000 samples from  $[-4, 4]^2$  for 30,000 epochs.

- **Four minima.** We place four minima at  $\mu = \{(2, 3), (3, -2), (-2, -3), (-1.5, 1.5)\}$ , with  $a_j = 0.25$  and  $v_j = 0.75$ . The process has  $\xi = 0.6$ ,  $\alpha = 2.5$  and  $\sigma = 0.225$ . We train a RNN with  $N = 128$  and 25,000 samples from  $[-4, 4]^2$  for 30,000 epochs.
- **Five minima.** We place five minima at  $\mu = \{(3.5, 4), (0, 0), (3, -4), (-3, 4), (-3.5, 4)\}$ , with  $a_j = 0.25$  and  $v_j = 0.6$ . The process has  $\xi = 0.6$ ,  $\alpha = 2.5$  and  $\sigma = 0.225$ . We train a RNN with  $N = 128$  and 40,000 samples from  $[-8, 8]^2$  for 40,000 epochs.

In Sec. IV, we retrain the second layers using 25,000 additional samples and 30,000 epochs to obtain the HHD.

### 3. Non-coplanar examples

In App. D, we use the following parameters.

- **Pixel images.** We fix minima at the points corresponding to the images, with Gaussian wells specified by  $a_j = 7, v_j = 11$ . The process has  $\sigma = 0.3$ ,  $\xi = 0.5$ ,  $s = -3.2$ , and  $\alpha = 40$ .
- **Points on the saddle.** We place points at the positions

given by,

$$\mu = \begin{pmatrix} 0.4 & 0.7 & 0.2 \\ 1 & -0.5 & -0.2 \\ -0.2 & -0.6 & 0.4 \\ -0.5 & 0.2 & -0.6 \end{pmatrix}, \quad (H1)$$

and take  $r_{\max} = 0.4$ ,  $\xi = 0.75$  and compute the curl with  $\Delta = 10^{-5}$ . The Gaussian wells are given by  $a_j = 0.5, v_j = 0.325$  and the process has  $\sigma = 0.155$  and  $\alpha = 4000$ .

### 4. Network asymmetry and entropy production

In App. F, we train RNNs with  $N = 64$  with 25,000 samples in  $[-4, 4]^2$  for 30,000 epochs and set  $\sigma = 0.25$ .

### 5. Measuring complexity of chaotic attractors

In App. G, we train RNNs with  $N = 1024$  with 125,000 samples for 2000 epochs using batches of size 1024. For the Halvorsen attractor, we take the samples in the range  $[-15, 12]^3$ . For the Rössler attractor, we take  $[-15, 12] \times [-15, 12] \times [0, 25]$ .

---

[1] M. W. Mathis, A. P. Rotondo, E. F. Chang, A. S. Tolias, and A. Mathis, “Decoding the brain: From neural representations to mechanistic models,” *Cell*, vol. 187, no. 21, pp. 5814–5832, 2024.

[2] S. Vyas, M. D. Golub, D. Sussillo, and K. V. Shenoy, “Computation through neural population dynamics,” *Annual Review of Neuroscience*, vol. 43, 2020.

[3] C. Pandarinath, D. J. O’Shea, J. Collins, R. Jozefowicz, S. D. Stavisky, J. C. Kao, E. M. Trautmann, M. T. Kaufman, S. I. Ryu, L. R. Hochberg, J. M. Henderson, K. V. Shenoy, L. F. Abbott, and D. Sussillo, “Inferring single-trial neural population dynamics using sequential auto-encoders,” *Nature Methods*, vol. 15, p. 805–815, 2018.

[4] D. Durstewitz, G. Koppe, and M. I. Thurm, “Reconstructing computational system dynamics from neural data with recurrent neural networks,” *Nature Reviews Neuroscience*, vol. 24, p. 693–710, 2023.

[5] D. Sussillo and L. F. Abbott, “Generating coherent patterns of activity from chaotic neural networks,” *Neuron*, vol. 63, no. 4, pp. 544–557, 2009.

[6] G. Hennequin, T. P. Vogels, and W. Gerstner, “Optimal control of transient dynamics in balanced networks supports generation of complex movements,” *Neuron*, vol. 82, no. 6, pp. 1394–1406, 2014.

[7] D. J. Gauthier, E. Boltt, A. Griffith, and W. A. S. Barbosa, “Next generation reservoir computing,” *Nature Communications*, vol. 12, no. 5564, 2021.

[8] J. Z. Kim and D. S. Bassett, “A neural machine code and programming framework for the reservoir computer,” *Nature Machine Intelligence*, vol. 5, pp. 622–630, 2023.

[9] L.-W. Kong, G. A. Brewer, and Y.-C. Lai, “Reservoir-computing based associative memory and itinerancy for complex dynamical attractors,” *Nature Communications*, vol. 15, no. 4840, 2024.

[10] J. Hopfield, “Neural networks and physical systems with emergent collective computational abilities,” *Proceedings of the National Academy of Sciences*, vol. 79, pp. 2554–2558, 1982.

[11] J. Hopfield, “Neurons with graded response have collective computational properties like those of two-state neurons,” *Proceedings of the National Academy of Sciences*, vol. 81, pp. 3088–3092, 1984.

[12] G. Pavliotis, *Stochastic Processes and Applications: Diffusion Processes, the Fokker-Planck and Langevin Equations*. Springer, 2014.

[13] D. J. Amit, *Modeling Brain Function: The World of Attractor Neural Networks*. Cambridge University Press, 1989.

[14] M. Khona and I. R. Fiete, “Attractor and integrator networks in the brain,” *Nature Reviews Neuroscience*, vol. 23, p. 744–766, 2022.

[15] H. Sompolinsky and I. Kanter, “Temporal association in asymmetric neural networks,” *Physical Review Letters*, vol. 57, no. 2861, 1986.

[16] J. A. Hertz, G. Grinstein, and S. A. Solla, “Irreversible spin glasses and neural networks,” in *Heidelberg Colloquium on Glassy Dynamics*. Springer, 2006.

[17] A. Crisanti and H. Sompolinsky, “Dynamics of spin systems with randomly asymmetric bonds: Langevin dynamics and a spherical model,” *Physical Review A*, vol. 36, no. 4922, 1987.

[18] H. Yan, L. Zhao, L. Hu, X. Wang, E. Wang, and J. Wang, “Nonequilibrium landscape theory of neural networks,” *Proceedings of the National Academy of Sciences*, vol. 100, no. 45, 2013.

[19] R. Nartallo-Kaluarachchi, M. Kringselbach, G. Deco, R. Lambotte, and A. Goriely, “Nonequilibrium physics of brain dynamics,” *Physics Reports*, vol. 1152, pp. 1–43, 2026.

[20] A. K. Behera, M. Rao, S. Sastry, and S. Vaikuntanathan, “Enhanced associative memory, classification, and learning with active dynamics,” *Physical Review X*, vol. 13, no. 041043, 2023.

[21] T. Spisak and K. Friston, “Self-orthogonalizing attractor neural networks emerging from the free energy principle,” *arXiv*, vol. 2505.22749, 2025.

[22] M. Aguilera, D. D. Martino, I. Garashchuk, and D. Sinelshchikov, “Nonequilibrium thermodynamics of associative memory continuous-time recurrent neural networks,” in *ALIFE 2025: Ciphers of Life: Proceedings of the Artificial Life Conference 2025*, 2025.

[23] A. Coolen, “Statistical mechanics of recurrent neural networks I—Statics,” in *Handbook of Biological Physics*, vol. 4, pp. 553–618, Elsevier, 2001.

[24] A. Coolen, “Statistical mechanics of recurrent neural networks II — Dynamics,” in *Handbook of Biological Physics*, vol. 4, pp. 619–684, Elsevier, 2001.

[25] M. G. Perich, D. Narain, and J. A. Gallego, “A neural manifold view of the brain,” *Nature Neuroscience*, vol. 28, p. 1582–1597, 2025.

[26] J. A. Gallego, M. G. Perich, L. E. Miller, and S. A. Solla, “Neural manifolds for the control of movement,” *Neuron*, vol. 94, no. 5, pp. 978–984, 2017.

[27] D. Sussillo and O. Barak, “Opening the black box: low-dimensional dynamics in high-dimensional recurrent neural networks,” *Neural Computation*, vol. 25, no. 3, pp. 626–649, 2013.

[28] F. Mastrogiovanni and S. Ostoic, “Linking connectivity, dynamics, and computations in low-rank recurrent neural networks,” *Neuron*, vol. 99, no. 3, pp. 609–623, 2018.

[29] V. Schmutz, A. Haydaroglu, S. Wang, Y. Feng, M. Carandini, and K. D. Harris, “High-dimensional neuronal activity from low-dimensional latent dynamics: a solvable model,” in *39th Conference on Neural Information Processing Systems (NeurIPS 2025)*, vol. 38, 2025.

[30] V. Thibeault, A. Allard, and P. Desrosiers, “The low-rank hypothesis of complex systems,” *Nature Physics*, vol. 20, pp. 294—302, 2024.

[31] B. Prasse and P. V. Mieghem, “Predicting network dynamics without requiring the knowledge of the interaction graph,” *Proceedings of the National Academy of Sciences*, vol. 119, no. 44, 2022.

[32] C. Fefferman, S. Mitter, and H. Narayanan, “Testing the manifold hypothesis,” *Journal of the American Mathematical Society*, vol. 29, pp. 983–1049, 2016.

[33] R. Mitchell-Heggs, S. Prado, G. P. Gava, M. A. Go, and S. R. Schultz, “Neural manifold analysis of brain circuit dynamics in health and disease,” *Journal of Computational Neuroscience*, vol. 51, pp. 1–21, 2023.

[34] D. V. Buonomano, G. Buzsáki, L. Davachi, and A. C. Nobre, “Time for memories,” *Journal of Neuroscience*, vol. 43, no. 45, pp. 7565–7574, 2023.

[35] H. Jaeger, “The “echo state” approach to analysing and training recurrent neural networks,” tech. rep., GMD Report 148, German National Research Center for Information Technology, 2001.

[36] C. Eliasmith and C. H. Anderson, *Neural Engineering: Computation, Representation and Dynamics in Neurobiological Systems*. MIT Press, 2003.

[37] P. J. Werbos, “Backpropagation through time: what it does and how to do it,” *Proceedings of the IEEE*, vol. 78, no. 10, pp. 1550–1560, 1990.

[38] Y. Bengio, P. Simard, and P. Frasconi, “Learning long-term dependencies with gradient descent is difficult,” *IEEE Transactions on Neural Networks*, vol. 5, no. 2, pp. 157–166, 1994.

[39] K. Hornik, M. Stinchcombe, and H. White, “Multilayer feedforward networks are universal approximators,” *Neural Networks*, vol. 2, no. 5, pp. 359–366, 1989.

[40] I. Goodfellow, Y. Bengio, and A. Courville, *Deep Learning*. MIT Press, 2016.

[41] E. Glötzl and O. Richters, “Helmholtz decomposition and potential functions for n-dimensional analytic vector fields,” *Journal of Mathematical Analysis and Applications*, vol. 525, no. 2, p. 127138, 2023.

[42] L. D. Costa and G. A. Pavliotis, “The entropy production of stationary diffusions,” *Journal of Physics A: Mathematical and Theoretical*, vol. 56, no. 36, p. 365001, 2023.

[43] M. H. Duong and M. Ottobre, “Non-reversible processes: GENERIC, hypocoercivity and fluctuations,” *Nonlinearity*, vol. 36, no. 1617, 2023.

[44] J. C. Sprott, *Elegant Chaos: Algebraically Simple Chaotic Flows*. World Scientific, 2010.

[45] S. Dadras and H. R. Momeni, “A novel three-dimensional autonomous chaotic system generating two, three and four-scroll attractors,” *Physics Letters A*, vol. 373, pp. 3637–3642, 2009.

[46] K. Pearson, “LIII. On lines and planes of closest fit to systems of points in space,” *The London, Edinburgh, and Dublin Philosophical Magazine and Journal of Science*, vol. 2, no. 11, pp. 559–572, 1901.

[47] M. M. Churchland, J. P. Cunningham, M. T. Kaufman, J. D. Foster, P. Nuyujukian, S. I. Ryu, and K. V. Shenoy, “Neural population dynamics during reaching,” *Nature*, vol. 487, p. 51–56, 2012.

[48] J. P. Cunningham and B. M. Yu, “Dimensionality reduction for large-scale neural recordings,” *Nature Neuroscience*, vol. 17, p. 1500–1509, 2014.

[49] C. J. Cuevas, A. Ardalani, M. Tsodyks, and N. Qian, “Recurrent neural network models for working memory of continuous variables: activity manifolds, connectivity patterns, and dynamic codes,” *arXiv*, vol. 2111.01275, 2021.

[50] R. Vidal, Y. Ma, and S. S. Sastry, *Generalized Principal Component Analysis*. Springer, 2016.

[51] K. Friston and P. Ao, “Free energy, value, and attractors,” *Computational and Mathematical Methods in Medicine*, vol. 2012, no. 937860, 2011.

[52] Y. LeCun, S. Chopra, R. Hadsell, M. Ranzato, and F. J. Huang, “Energy-based models,” in *Predicting Structured Data*, MIT Press, 2007.

[53] R. Nartallo-Kaluarachchi, M. Asllani, G. Deco, M. L. Kringselbach, A. Goriely, and R. Lambiotte, “Broken detailed balance and entropy production in directed networks,” *Physical Review E*, vol. 110, no. 034313, 2024.

[54] M. Fruchart, R. Hanai, P. B. Littlewood, and V. Vitelli, “Nonreciprocal phase transitions,” *Nature*, vol. 592, pp. 363–369, 2021.

[55] H. Ninou, J. Kadmon, and N. A. Cayco-Gajic, “Curl descent: Non-gradient learning dynamics with sign-diverse plasticity,” in *39th Conference on Neural Information Processing Systems (NeurIPS 2025)*, 2025.

[56] D.-Q. Jiang, M. Qian, and M.-P. Qian, *Mathematical Theory of Nonequilibrium Steady States: On the Frontier of Probability and Dynamical Systems*. Springer, 2004.

[57] V. I. Bogachev, *Measure Theory*. Springer, 2007.

[58] E. Pollock and M. Jazayeri, “Engineering recurrent neural networks from task-relevant manifolds and dynamics,” *PLOS Computational Biology*, vol. 16, no. 8, p. e1008128, 2020.

[59] R. B. Yishai, R. L. Bar-Or, and H. Sompolinsky, “Theory of orientation tuning in visual cortex,” *Proceedings of the National Academy of Sciences*, vol. 92, pp. 3844–3848, 1995.

[60] A. D. Bernardo, A. Valente, F. Mastrogiovise, and S. Ostoic, “Shaping manifolds in equivariant recurrent neural networks,” *arXiv*, vol. 2511.04802v2, 2025.

[61] K. Rajan, C. D. Harvey, and D. W. Tank, “Recurrent network models of sequence generation and memory,” *Neuron*, vol. 90, no. 1, pp. 128–142, 2016.

[62] M. Aguilera, M. Igarashi, and H. Shimazaki, “Nonequilibrium thermodynamics of the asymmetric Sherrington-Kirkpatrick model,” *Nature Communications*, vol. 14, no. 3685, 2023.

[63] M. Aguilera, S. A. Moosavi, and H. Shimazaki, “A unifying framework for mean-field theories of asymmetric kinetic Ising systems,” *Nature Communications*, vol. 58, 2021.

[64] C. W. Lynn, C. M. Holmes, W. Bialek, and D. J. Schwab, “Decomposing the local arrow of time in interacting systems,” *Physical Review Letters*, vol. 129, no. 118101, 2022.

[65] Y.-A. Ma, T. Chen, and E. B. Fox, “A complete recipe for stochastic gradient MCMC,” in *NIPS’15: Proceedings of the 29th International Conference on Neural Information Processing Systems*, vol. 2, pp. 2917–2925, 2015.

[66] P. Kloeden and E. Platen, *Numerical Solution of Stochastic Differential Equations*. Springer, 1992.

[67] T. Hastie, R. Tibshirani, and J. Friedman, *The Elements of Statistical Learning: Data Mining, Inference, and Prediction*. Springer, 2009.

[68] P. Virtanen, R. Gommers, T. E. Oliphant, M. Haberland, T. Reddy, D. Cournapeau, E. Burovski, P. Peterson, W. Weckesser, J. Bright, S. J. van der Walt, M. Brett, J. Wilson, K. J. Millman, N. Mayorov, A. R. J. Nelson, E. Jones, R. Kern, E. Larson, C. J. Carey, İlhan Polat, Y. Feng, E. W. Moore, J. VanderPlas, D. Laxalde, J. Perktold, R. Cimrman, I. Henriksen, E. A. Quintero, C. R. Harris, A. M. Archibald, A. H. Ribeiro, F. Pedregosa, P. van Mulbregt, and S. . Contributors, “Scipy 1.0: fundamental algorithms for scientific computing in Python,” *Nature Methods*, no. 17, p. 261–272, 2020.

[69] M. P. do Carmo, *Differentiable Geometry of Curves and Surfaces*. Prentice-Hall, 1976.

[70] J. M. Lee, *Introduction to Smooth Manifolds*. Springer, 2000.

[71] R. Nartallo-Kaluarachchi, R. Lambiotte, and A. Goriely, “Coarse-graining nonequilibrium diffusions with Markov chains,” *arXiv*, vol. 2511.05366, 2025.